PHYSICAL REVIEW FLUIDS **5**, 074605 (2020)

Characteristics of fluctuating wall-shear stress in a turbulent boundary layer at low-to-moderate Reynolds number

Jianjie Wang,[1] Chong Pan,[1,2,*] and Jinjun Wang[1]
[1] *Key Laboratory of Fluid Mechanics of Ministry of Education, Beihang University, Beijing 100191, China*
[2] *Aircraft and Propulsion Laboratory, Ningbo Institute of Technology,*
Beihang University, Ningbo 315100, China

(Received 19 February 2020; accepted 25 June 2020; published 20 July 2020)

The present work deals with the characteristics of the streamwise component of the fluctuating wall-shear stress τ_w' in a smooth-wall turbulent boundary layer. A near-wall two-dimensional time-resolved particle image velocimetry measurement was performed in a low-to-moderate Reynolds number range ($\mathrm{Re}_\tau = 400 \sim 2900$). The algorithm of single-row cross correlation, together with a newly proposed iterative fitting method, was used to estimate τ_w' from instantaneous near-wall velocity fields at single pixel row resolution. Additionally, existing direct numerical simulation datasets in the same Re_τ range were also analyzed for direct comparison. The fluctuating intensity of τ_w' is found to follow the empirical log-law correlation, i.e., $\sigma_{\tau_w}^+ \propto \ln \mathrm{Re}_\tau$. This indicates the existence of the influence of outer-layer large-scale or very-large-scale motions (LSMs or VLSMs) on the wall. The following scale decomposition analysis suggests an inner-scaling nature of the cutting-off boundary between small- and large-scale components of τ_w', the magnitude of which is $\lambda_{xc}^+ \approx 1000$, equivalent to the mean streamwise length of near-wall streaky structures. Combining with the weak Re-dependency of both the skewness of τ_w' and its convection speed, i.e., $S_{\tau_w} \approx 1$ and $\overline{u_c}^+ \approx 12$, it can be inferred that in the present studied Re range, LSMs or VSLMs only leave a mild footprint on the wall. Instead, the amplitude modulation effect is inferred to play a more prominent role in affecting both the statistics and the multiscale characteristics of τ_w'.

DOI: 10.1103/PhysRevFluids.5.074605

I. INTRODUCTION

Wall-shear stress (abbreviated as "WSS" hereinafter) is generated by the relative motion between the no-slip wall and the viscous fluid flowing over it. For streamlined vehicles, such as aircrafts and ships, WSS contributes a significant portion of the total drag force, making it an important factor to be considered when assessing or controlling the aerodynamic performance in a wide range of industry applications [1]. Hereinafter, only the streamwise component of WSS, denoted as τ_w (with the subscript x being explicitly omitted), is focused, since it is this component that mainly contributes to the skin friction.

A. Re-dependency of the statistics of WSS

In fundamental research, detailed knowledge on WSS is of vital importance in characterizing wall-bounded turbulence [2], the reason is that the mean WSS, i.e., $\overline{\tau_w}$, determines the friction velocity and the inner length scale of turbulent motions by $u_\tau = \sqrt{\overline{\tau_w}/\rho}$ and $l^* = \nu/u_\tau$ (with ρ and

---

[*] panchong@buaa.edu.cn

TABLE I. Summary of previous studies on the statistics of WSS.

Work	Flow type	Re range	Method	Symbol[a]	$\sigma^+_{\tau_w}$	S_{τ_w}
Alfredsson *et al.* [12]	TBL	$\mathrm{Re}_\delta = 28000$[b]	flush-mounted hot wire	none	0.39	1
	TCF	$\mathrm{Re}_h = 3800/5000$[c]	flush-mounted hot film		0.36/0.35	1.1/0.9
Österlund [30]	TBL	$\mathrm{Re}_\theta = 2500 \sim 9800$[d]	HWA	▶	0.36∼0.4	not given
Miyagi *et al.* [18]	TCF	$\mathrm{Re}_h = 8758 \sim 17517$	micro shear stress imaging chip	none	0.4	1
Keirsbulck *et al.* [19]	TCF	$\mathrm{Re}_\tau = 74 \sim 400$	electrochemical probe	■	0.32∼0.40	0.91∼1.17
Mathis *et al.* [29]	TBL	$\mathrm{Re}_\tau = 4480$	HWA	◁	0.4	1
Willert [31]	TBL	$\mathrm{Re}_\tau = 240$	PIV	◀	0.41	0.80
Li *et al.* [32]	TBL	$\mathrm{Re}_\theta = 1009 \sim 4070$	μ-PTV	▼	0.39∼0.43	not given
Gubian *et al.* [20]	TCF	$\mathrm{Re}_\tau = 230 \sim 950$	flush-mounted HWA	○	0.28∼0.44	1.13∼1.44
Liu *et al.* [21]	TCF	$\mathrm{Re}_\tau = 860/1300$	micro pillar sensor	□	0.28/0.29	0.88/1.3
Abe *et al.* [23]	TCF	$\mathrm{Re}_\tau = 180/395/640$	DNS	◇	log-law	not given
Hu *et al.* [24]	TCF	$\mathrm{Re}_\tau = 90 \sim 1440$	DNS	▲	log-law	0.96∼1.14
Schlatter and Örlü [22]	TBL	Re_θ=500–4300	DNS	★	log-law	not given
Lee and Moser [25]	TCF	$\mathrm{Re}_\tau = 180 \sim 5186$	DNS	△	log-law	not given
Diaz-Daniel *et al.* [26]	TBL	$\mathrm{Re}_\tau = 409 \sim 625$	DNS	▷	log-law	0.94∼1.03
				- - - - -		

[a] Symbols listed in this table are used in Fig. 10 for the related work.
[b] $\mathrm{Re}_\delta = \delta U_\infty/\nu$, U_∞ is free-stream velocity.
[c] $\mathrm{Re}_h = hU_\infty/\nu$, h is the channel half-height.
[d] $\mathrm{Re}_\theta = \theta U_\infty/\nu$, θ is the momentum deficit thickness.

ν the density and kinematic viscosity of the fluid, respectively). The long debate on the exact value of Kármán constant κ adds weight to the need for an accurate measurement of WSS [3]. The scaling of WSS itself is also an interesting issue, since it is an intuitive measure of the asymptotic state of high Re effect. Evaluating the effect of roughness wall on near-wall turbulence also requires full access to the statistics of WSS [4]. Furthermore, the kinematics of WSS is expected to cast light on the mechanisms of the laminar-to-turbulent transition in wall-bounded flows [5].

Up to now, mean WSS and its Re-dependency in a canonical wall-bounded turbulence, such as turbulent boundary layer (TBL) and turbulent channel flow (TCF), has been well documented with high precision by means of either experimental measurement or numerical simulation [6]. In contrast, the statistics of the fluctuating WSS, especially its multiscale characteristics, receives comparably less attention. Knowledge on this issue is expected to promote the understandings on the generation mechanism of wall skin friction [7,8], as well as to inspire the development of physical-based wall model in large-eddy simulation (LES) [9,10]. It also serves as a practical indicator for active turbulent flow control [11].

Traditional view on the fluctuating WSS is that its root-mean-squared (RMS) value, being normalized by the mean value, is a constant of $\sigma^+_{\tau_w} = \sigma_{\tau_w}/\overline{\tau_w} = 0.4$. This is supported by early studies in both TBL [12–16] and TCF [17,18]. Table I summarizes typical studies on the statistics of WSS in wall-bounded turbulence by either experimental or numerical methods. As shown in Table I, recent experiments with the aid of specially designed high-resolution sensors reported a scattered $\sigma^+_{\tau_w}$ ranging from 0.2 to 0.45 in low Re TCF [19–21]. Meanwhile, a direct numerical simulation (DNS) of a TBL suggested a logarithmic dependency of $\sigma^+_{\tau_w}$ on the frictional Reynolds number $\mathrm{Re}_\tau = \delta u_\tau/\nu$ (with δ the 99% boundary layer thickness), i.e., $\sigma^+_{\tau_w} = 0.298 + 0.018 \ln \mathrm{Re}_\tau$ [22]. This log-law dependency was further supported by other DNS studies in both TCF [23–25] and TBL [26].

Such a log-law correlation might suggest the increased contribution of large-scale motions or very-large-scale motions (LSMs/VLSMs) originated from the log layer and above to the fluctuation strength of WSS at the wall [23,27–29]. However, the validation of this log-law Re-dependency in high Re scenario, especially by experimental approaches, is still lacked. Additionally, Table I shows a scattered distribution of the skewness of WSS (denoted as S_{τ_w}), which seems to center around 1. But Diaz-Daniel *et al.* [26] recently reported a weak Re-dependency of S_{τ_w} in the low-Re regime, they attributed it to the increased intermittency with the increase of Re_τ. On considering the slow convergence nature of high-order moments, whether S_{τ_w} presents a Re-dependency is an intriguing issue to be studied.

B. Experiment method for WSS measurement

In general, the techniques of WSS measurement can be divided into two groups, one is the direct force measurement and the other is the indirect methods. The most popular direct approach is the floating-element force balance. Without the need of calibration, this method was found to behave well in various aerodynamic applications [33,34]. Nevertheless, the measurement uncertainty is associated with sensor misalignment, system inertia or the pressure gradient. Even though the sensor could be fabricated into micro scale nowadays [35], the uncertainty and the reliability of this method is case dependent, and the practical implementation requires full experience [36,37]. As for the indirect branch, a commonly used method is to measure the heat transfer rate at the wall via flush-mounted hot wire anemometer (HWA) [20]), hot film [27] or micro-electromechanical-systems (MEMS) thermal sensors [38]. This method suffers from bias from the heat loss to the substrate [12]. The interference effect between the sensor and the wall is complex for a precise quantification. This issue becomes more critical in high Re case where the viscous sublayer is much thinner.

An alternative approach is to estimate WSS based on assumptions of the law of the wall for near-wall mean velocity profile. The linear law of $\overline{U}^+ = y^+$ (the superscript + indicates inner scaling, i.e., $\overline{U}^+ = \overline{U}/u_\tau$ and $y^+ = y/l^*$, while the overline indicates an ensemble average) is the one being invoked the most frequently. It applies for the viscous sublayer with $y^+ \leqslant 5$, where the velocity gradient is assumed to be constant [39]. A simple least-squares fitting can then be taken to estimate the average velocity gradient (and the WSS at the wall). Örlü *et al.* [40] suggested an extended linear law (with additional fourth- and fifth-order polynomial terms) till $y^+ = 10 \sim 15$ to incorporate more points into the fitting. But additional coefficients in the polynomial should be calibrated in advance.

The accuracy of velocity-gradient-based methods relies on two aspects, the precision of the near-wall velocity measurement and the number of points being included in the fitting. The latter puts critical requirement on the spatial resolution of the instrumentation, especially in high Re scenario. The techniques of particle image velocimetry (PIV) and particle tracking velocimetry (PTV) have shown their potential in the near-wall measurements owing to their non-intrusive feature [15,31,32,41–44]. Comparing to PIV, PTV tracks the displacement of individual particles so that is superior in spatial resolution. Sheng *et al.* [15] measured the spatial distribution of WSS in a TBL at $\mathrm{Re}_\tau = 1470$ using digital holographic microscope technique combined with PTV. Li *et al.* [32] developed a μ-PTV system to study the statistics of the fluctuating WSS in a zero-pressure-gradient (ZPG) TBL at $\mathrm{Re}_\theta = 1009 \sim 4070$. They reported a logarithmic law of $\sigma^+_{\tau_w} = 0.2037 + 0.0274 \ln \mathrm{Re}_\tau$ that is only slightly different from the one being proposed by Schlatter and Örlü [22] via DNS. Rowin and Ghaemi [45] recently applied three-dimensional (3D) Lagrangian PTV to measure near-wall turbulent flow over a superhydrophobic surface in a TCF. The mean skin friction, as well as the slip length introduced by the superhydrophobic surface, was then estimated by the mean velocity gradient below the viscous sublayer. The limitation of PTV, to our knowledge, is that the particle matching accuracy is sensitive to the setting parameters in the particle detecting and tracking procedure [46].

Window-based cross-correlation (WC) algorithm used in PIV is comparably more robust due to the nature of tracking the translation of a group of particles. Nevertheless, the reduced spatial resolution, which is determined by the size of the interrogation window (IW), will bias the velocity gradient in the vicinity of the wall. To overcome this limitation, Kähler *et al.* [41] developed a method of single pixel ensemble correlation (SPEC) to resolve ensemble-averaged velocity vector at single pixel resolution by averaging the cross-correlation map of pixel-wise IW across a large bulk of ensemble. They incorporated this method in a μ-PIV system to perform reliable measurement of near-wall mean velocity profile. The robustness and accuracy of the SPEC algorithm in estimating mean WSS was further investigated by Shen *et al.* [43]. The limitation of this method is that the temporal information is scarified as a price of high spatial resolution.

Attempts have also been taken to measure instantaneous WSS via PIV-based algorithm. Nguyen and Wells [47] proposed a technique of PIV/interface gradiometry (PIV/IG), which directly measures the instantaneous velocity gradient at the wall via linearly shearing the IW at the no-slip wall before cross-correlating it with the next frame. A rectangle IW with large aspect ratio, instead of a square one in conventional PIV, was used to enhance the wall-normal resolution. Nguyen *et al.* [48] further proposed an interfacial PIV (IPIV) technique to resolve the near-wall velocity over a curved surface at single row resolution in wall-normal direction. After prestretching the image to straighten the curved wall via conformal transformation, one-dimensional cross correlation was performed over each horizontal pixel-row (served as IW) of the particle image, yielding the tangential velocity parallel to the wall. WSS could be then estimated by a least-squares fitting of the instantaneous velocity profile to the prescribed law of the wall. Such a single-row cross correlation (SRCC) technique was further utilized by Willert [31] in the measurement of instantaneous WSS in a TBL at $\mathrm{Re}_\tau = 240$ with IW size of 256×1 pixels. The yielded statistics of WSS were consistent with previous studies [12,22], as can be seen in Table I. Zhu *et al.* [44] recently developed a so-called joint-translation-shear-correlation (JTSC) algorithm as an extension of PIV/IG to resolve the near-wall velocity and its wall-normal gradient simultaneously. With a IW size of 256×32 pixels, JTSC was found to behave well in the near-wall measurement of a transitional boundary layer in both low-speed and high-Mach-number scenario.

C. Research purpose

The present study aims at studying the statistics of instantaneous WSS and its multiscale characteristics in a canonical TBL. The Re-dependency, as well as the scaling for small-scale and large-sale components of fluctuating WSS, is the primary issue to be discussed. With this purpose, time-resolved two-dimensional PIV (TR-2D PIV) was taken in the near-wall region that well extends into the viscous sublayer. The studied Re_τ covered a range of $400 \sim 2900$. The technique of SRCC was adopted for a reliable measurement of the near-wall instantaneous velocity profile due to its robustness to particle missing and noise contamination. An iterative fitting method was further proposed to estimate the instantaneous WSS by taking into account the temporal variation of the upper bound of the viscous sublayer. DNS datasets of a spatially developing ZPG-TBL obtained in Refs. [49–51] were also analyzed to provide a direct comparison to the experiment results.

The present studied TBL is described in Sec. II at first. A description of the PIV experiment and the data processing method is then introduced in Sec. III. Section IV analyzes the statistics of WSS, including the first three-order moments, the probability density function (PDF) and the convection speed. Section V deals with the multiscale characteristics of WSS by decomposing the time-series of fluctuating WSS into small- and large-scale components. Concluding remarks are finally given in Sec. VI.

II. DATASET DESCRIPTION AND FLOW-FIELD CALIBRATION

In this section, the characteristics of the present studied smooth-wall ZPG-TBLs are to be calibrated at first. Hereinafter, x, y, and z denotes the streamwise, wall-normal, and spanwise direction, respectively. $U/V/W$ are the corresponding velocity components. τ_w and τ_w' denote the streamwise component of the instantaneous and the fluctuating WSS, respectively.

A. Experiment dataset

In the experimental side, two measurements were taken. The first one was performed in a low-speed recirculating water tunnel in Beihang University, whose test section had a size of 18 m in length, 1 m in width, and 1.2 m in height. The turbulence intensity T_u was about 0.8% at a typical free-stream velocity $U_\infty = 0.5\,\mathrm{ms}^{-1}$. Five pieces of hydraulic-smooth Acrylic plates, each had a size of 3 m in length, 1 m in height and 20 mm in thickness, were assembled in together to form a 15-m-in-length flat plate, which was positioned vertically in the main test section to generate a smooth-wall TBL over it. Its leading edge had a 4:1 half-elliptical shape to avoid local flow separation. Transition was triggered by a 3-mm-in-diameter tripping wire glued onto the surface at 0.4 m downstream of the leading edge. The measurement position was located at 12 m downstream of the tripping wire, where the 99% boundary layer thickness δ was less than 0.36 m. The working surface was gaped 0.75 m away from the sidewall of the water tunnel, so that the effect of the side wall on the measured TBL was negligible. The water depth was 1 m, and the measured streamwise—wall-normal (x-y) plane was 0.5 m away from both the free water surface and the bottom wall to minimize the end effect. Figure 1(a) shows the sketch of the experiment setup. More details about this facility can be referred to Refs. [52,53].

By varying U_∞ from 0.038 to $0.359\,\mathrm{ms}^{-1}$, five Re_τ ranging from 600 $\sim$ 2900 were tested. They are marked as Case WT1 $\sim$ WT5, with "WT" abbreviating water tunnel. Due to the long developing length, there was minor favorable pressure gradient (FPG) in the tested TBL. The acceleration parameter $[K = (\nu/U_\infty^2)dU_\infty/dx]$ in the measurement domain was estimated to be smaller than 0.4×10^{-7}. As can be seen in Sec. II C, this minor FPG condition is insufficient to distinctly affect the turbulence statistics. Furthermore, Wang *et al.* [54] have demonstrated that it has little effect on the kinematics of near-wall low-speed streaks, which in turn have a tight correlation with WSS at the wall [26,55]. Therefore, such a minor FPG condition is inferred to have insignificant influence on the statistics of WSS. This will be demonstrated later by a comparison to DNS results.

In the second experiment, a TBL was developed on the bottom wall of a low-speed recirculating water channel. The test section of this facility had a size of 3 m in length, 0.6 m in width and 0.7 m in height, and was made of hydraulic-smooth glass for optical access. The turbulence intensity T_u was about 0.5% at a typical free-stream velocity of $U_\infty = 0.2\,\mathrm{ms}^{-1}$. The water depth was 0.50 m. A plexiglas plate with a size of 1.0 m in length and 0.6 m in width was hung on the top of the free water surface, covering the middle part of the test section, to suppress the surface wave. Boundary layer transition was triggered by a 3-mm-in-diameter tripping wire being placed at 0.1 m downstream of the test section inlet. The measured symmetric x-y plane was fixed at 1.73 m downstream of the tripping wire [as illustrated in Fig. 1(b)], where the fully developed turbulent state was guaranteed. The ZPG condition of this facility has been validated in Refs. [54,56]. Four cases labeled as WC1 $\sim$ WC4 ("WC" is short for water channel) were tested by increasing U_∞ from 0.074 to $0.377\,\mathrm{ms}^{-1}$, covering a Re_τ range of 400 $\sim$ 1800.

Figure 2 presents the wall-normal profiles of the mean streamwise velocity $\overline{U}^+(y^+)$ and the streamwise velocity fluctuation intensity $u^+_{\mathrm{rms}}(y^+)$ of all the experiment cases measured by one-dimensional Laser Doppler Velocimetry (1D-LDV, Dantec FlowExplorer). The size of the probing volume was 1.4 mm in the wall-normal direction, corresponding to 2 $\sim$ 20 wall units at various Re_τ. The friction velocity u_τ and the boundary layer thickness δ were estimated by a least-squares fitting of the yielded $\overline{U}^+(y^+)$ to the empirical composite velocity profile proposed in Ref. [57]. Table II summarizes the yielded u_τ and δ, as well as other characteristic parameters, i.e., the displacement thickness δ^*, the momentum deficit thickness θ and the characteristic Reynolds numbers, of all the studied cases (incuding the DNS cases to be described later).

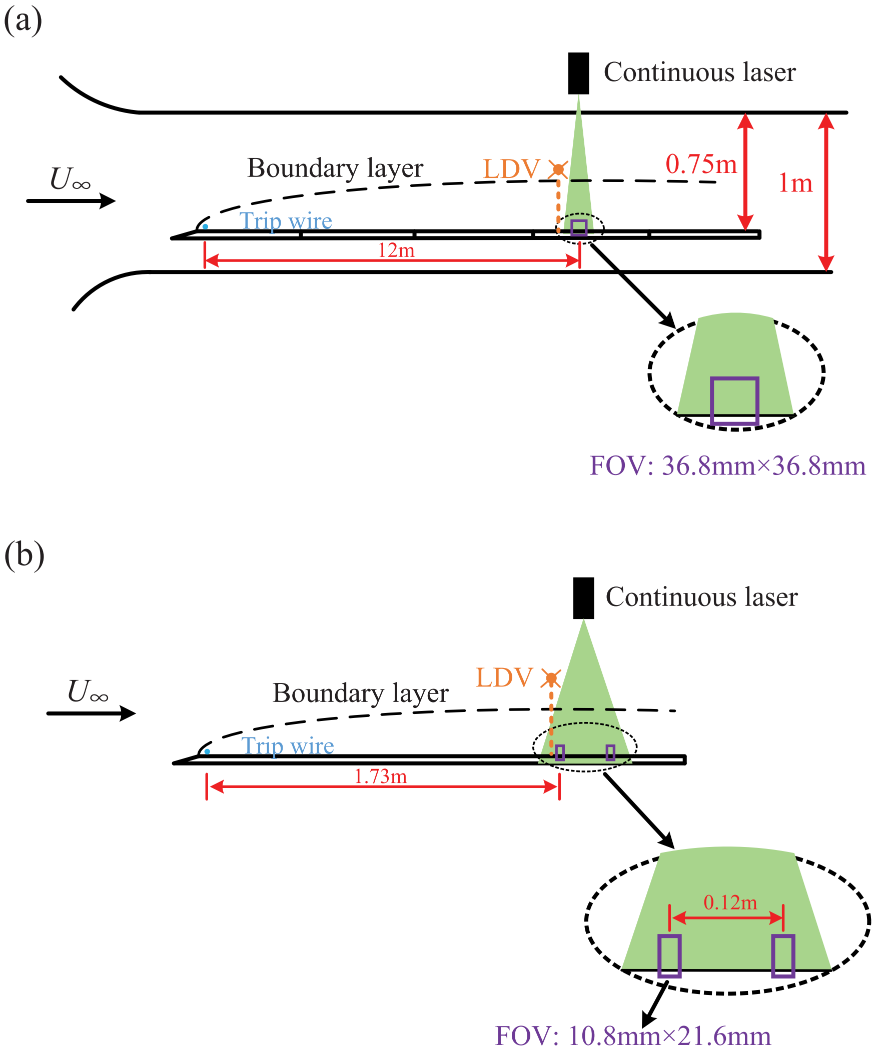

FIG. 1. Schematic illustration of PIV measurements in two facilities: (a) water tunnel (Case WT1 $\sim$ WT5); (b) water channel (Case WC1 $\sim$ WC4). The cross marker with a dot in each subfigure illustrates the probing position of 1D-LDV to monitor the free-stream velocity.

As shown in Fig. 2, all the $\overline{U}^+(y^+)$ profiles collapse well with each other in the logarithmic region and below. $u^+_{\mathrm{rms}}(y^+)$ of the experiment cases, however, suffer a systematic underestimation if compared to those of the DNS cases at similar Re_τ. This is attributed to the relatively large probing volume of the LDV measurement, which serves as a spatial average to smear out small-scale fluctuations.

B. DNS dataset

Five DNS datasets of a spatially developing smooth-wall TBL with $\mathrm{Re}_\tau = 600 \sim 2500$ were analyzed to provide a comparison to the experiment results. They are denoted as DNS1$\sim$DNS5. Two lower Re cases (DNS1$\sim$DNS2) and three higher ones (DNS3$\sim$DNS5) are truncated from the database of Simens *et al.* [49] and Sillero *et al.* [50,51], respectively, both of which are available

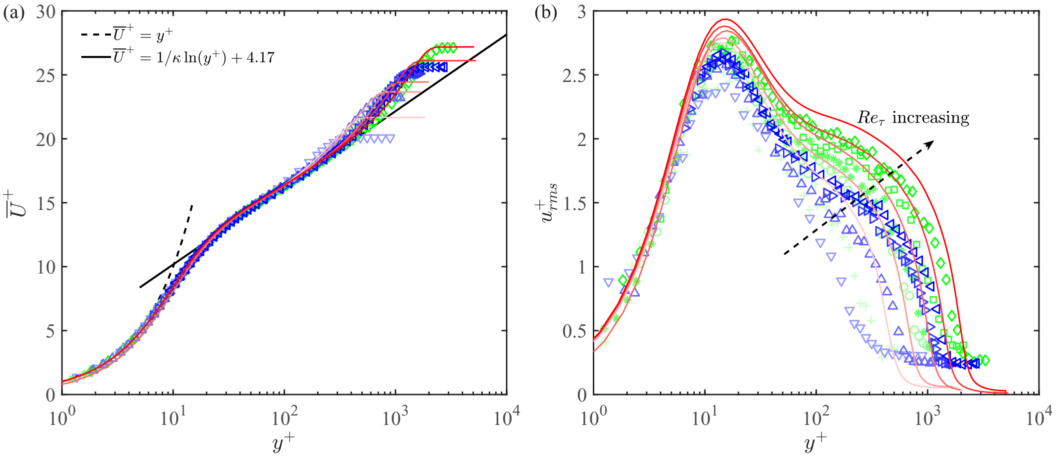

FIG. 2. Wall-normal profiles of (a) mean streamwise velocity $\overline{U}^+(y^+)$ and (b) streamwise velocity fluctuation intensity $u^+_{\mathrm{rms}}(y^+)$ measured by 1D-LDV. The DNS results are also shown. The black dashed and solid lines in (a) indicate the linear law and the log law, respectively. Symbol list is given in Table II. The Kármán constant takes the value of κ=0.384, the same in the following.

online (http://torroja.dmt.upm.es/ftp/blayers/). Each case contains 28 snapshots of instantaneous 3D volumetric velocity fields. For each snapshot, the whole volume was cut into 96 (in DNS1$\sim$DNS2) or 128 (in DNS3$\sim$DNS5) slices of side-view x-y planes, each of which had a streamwise span of 6δ and a wall-normal span of 1δ, and was sufficiently gaped in the spanwise direction for statistical independence. The whole ensemble contained 2688 slices in DNS1$\sim$DNS2 and 3584 ones in DNS3$\sim$DNS5. The profiles of $\overline{U}^+(y^+)$ and $u^+_{\mathrm{rms}}(y^+)$ at the middle of the streamwise span of the slice, where the nominal Re_τ is 400, 700, 1000, 1500, and 2000, respectively, are shown in

TABLE II. Summary of the characteristic boundary layer parameters of all the cases analyzed here. WT1 $\sim$ WT5 are the cases in the water tunnel test, WC1 $\sim$ WC4 the cases in the water channel test, DNS1$\sim$DNS2 the DNS cases from Simens *et al.* [49] and DNS3$\sim$DNS5 the cases from Sillero *et al.* [50,51].

Cases	U_∞(mm/s)	u_τ(mm/s)	δ(mm)	δ^*(mm)	θ(mm)	$\mathrm{Re}_\tau = \dfrac{\delta u_\tau}{\nu}$	$\mathrm{Re}_{\delta^*} = \dfrac{\delta^* U_\infty}{\nu}$	$\mathrm{Re}_\theta = \dfrac{\theta U_\infty}{\nu}$	Symbol[a]
WT1	37.8	1.8	341	36.4	25.4	600	1335	930	+
WT2	86.1	3.5	353	44.3	31.8	1215	3705	2665	○
WT3	147.9	5.9	257	32.3	23.4	1510	4760	3450	✳
WT4	169.6	6.5	310	38.9	28.5	1970	6420	4695	□
WT5	359.3	13.3	215	26.7	19.8	2840	9560	7070	◇
WC1	73.8	3.7	122	13.6	9.2	440	980	660	▽
WC2	139.3	6.0	157	19.8	14.0	870	2540	1800	△
WC3	258.1	10.3	159	20.2	14.6	1500	4760	3450	▷
WC4	377.3	14.7	131	16.4	12.0	1790	5730	4180	◁
DNS1	–	–	–	–	–	610	1420	990	—
DNS2	–	–	–	–	–	875	2540	1800	—
DNS3	–	–	–	–	–	1300	3970	2860	—
DNS4	–	–	–	–	–	1880	6405	4650	—
DNS5	–	–	–	–	–	2540	8870	6500	—

[a] The definition of the symbols is adopted in Figs. 2, 11, 12(e), 12(f) 14, and 15.

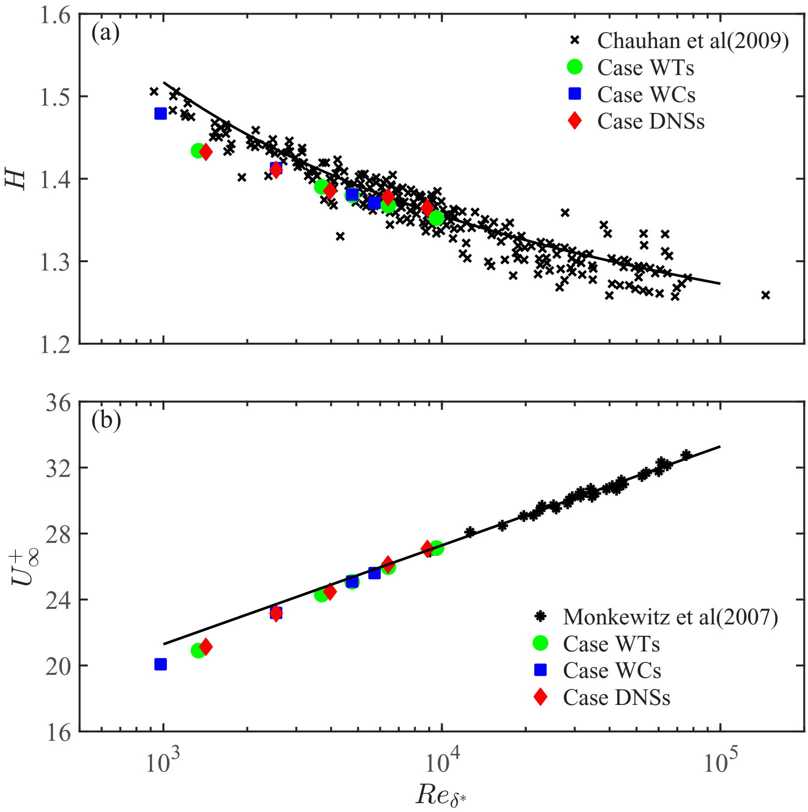

FIG. 3. The variation of (a) the shape parameter H and (b) the inner-scaled free-stream velocity U_∞^+ as a function of Re_{δ^*}. The symbols of × in (a) are reproduced from Fig. 5 in Ref. [57], and ✳ in (b) are reproduced from Fig. 3(a) in Ref. [59]. The solid lines in (a) and (b) indicate Eqs. (1) and (2), respectively.

Fig. 2. To keep consistency with the experiment cases, composite profile fitting was also taken here. It overestimates δ by about 20%, resulting in a 20% increase of the fitted Re_τ, as has been reported in Ref. [58]. In contrast, δ^* and θ are less affected by the composite fitting since they are integrated across the whole boundary layer.

C. Flow-field calibration

To calibrate the "canonical" state of the present studied TBL, the characteristic boundary layer parameters of all the cases are compared to those of the existing studies that have been summarized by Chauhan *et al.* [57] and Monkewitz *et al.* [59]. Figure 3 shows the variation of the shape factor H and the inner-scaled free-stream velocity U_∞^+ with respect to Re_{δ^*}. Except for the lowest Re cases (WC1, WT1, DNS1) that seem to suffer from the effect of insufficient transition, higher Re cases present acceptable accordance with the empirical correlations in Refs. [57,59], which are regarded to well characterize the "well-behaved" smooth-wall ZPG-TBL, i.e.,

$$H = \left[1 - \frac{7.11}{\kappa^{-1}\ln(\mathrm{Re}_{\delta^*}) + 3.3}\right]^{-1} + \frac{12}{\mathrm{Re}_{\delta^*}}, \tag{1}$$

$$U_\infty^+ = \frac{1}{\kappa}\ln(\mathrm{Re}_{\delta^*}) + 3.3, \text{ with } \kappa = 0.384. \tag{2}$$

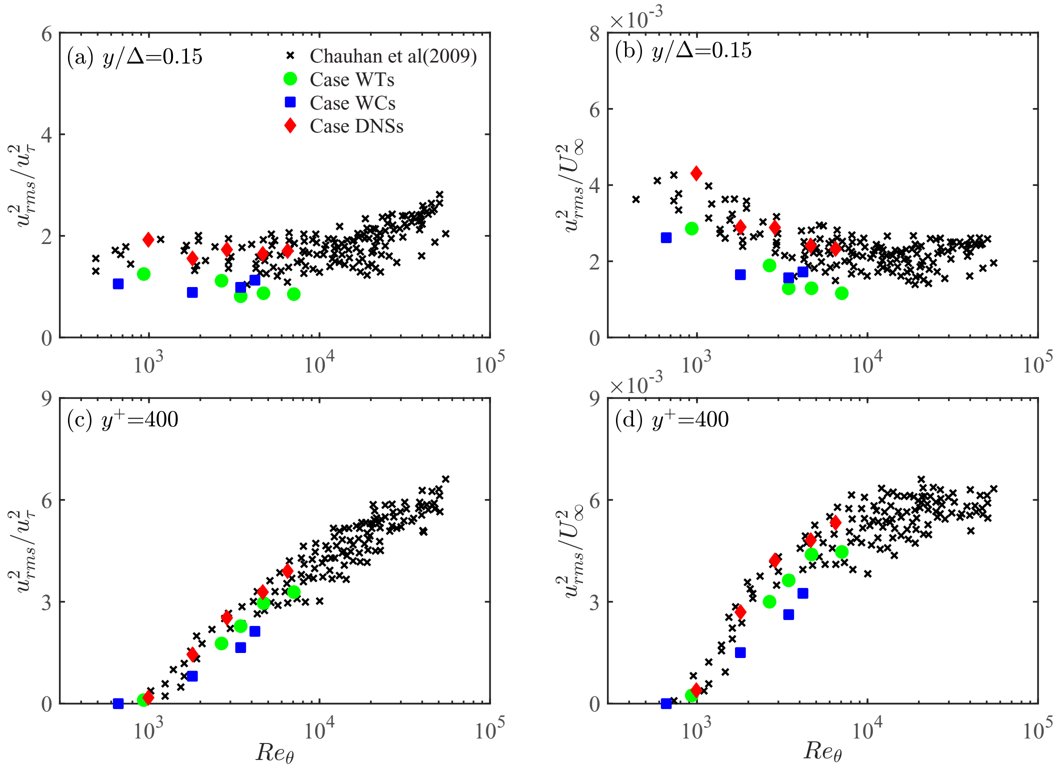

FIG. 4. The variation of u^2_{rms} at $y/\Delta = 0.15$ in (a, b) and $y^+ = 400$ in (c, d) as a function of Re_θ. u^2_{rms} are normalized by u^2_τ in (a, c) and U^2_∞ in (b, d). The symbols of × are reproduced from Fig. 8 in Ref. [57].

Furthermore, u_{rms} in both inner-scaling and outer-scaling at two typical wall-normal heights, i.e., $y = 0.15\Delta$ ($\Delta = U^+_\infty \delta^*$ is the Clauser length scale) and y^+=400, are plotted in Fig. 4 as a function of Re_θ. Due to the insufficient spatial resolution in the LDV measurement, the magnitudes of the experiment cases are found to be lower than both those of the DNS cases and the existing values summarized in Ref. [57]. Nevertheless, the overall trend of $u^2_{\mathrm{rms}} \sim \mathrm{Re}_\theta$ is similar. Recalling that the LDV results are not used in the following analysis; therefore, there is no necessary to compensate this resolution limitation. Furthermore, it is stressed that the minor effect of the FDG condition in Case WTs can be evidenced by the fact that their characteristic boundary layer parameters, i.e., H, U^+_∞, and u_{rms}, are consistent with those in both Case WCs and Case DNSs.

III. METHOD OF WSS ESTIMATION

This section describes the details of the WSS measurement, including the PIV implementation, the SRCC algorithm and the iterative linear fitting method. The measurement uncertainty and systematical bias are also evaluated.

A. Near-wall PIV measurement

TR-2D PIV is used to measure the near-wall velocity fields in two facilities being described in Sec. II A. The optical setup for the near-wall measurement is illustrated in Fig. 1. The flow fields were seeded by hollow glass beads with a mean diameter of 10 μm and a density of 1.05 g mm^{-2}. A 1-mm-in-thickness continuous laser sheet with an energy output of 8 w and a wavelength of 532 nm illuminated the near-wall region of the symmetric x-y plane at the desired x station. Particle images

TABLE III. Parameters of the PIV experiment, together with the estimated error of the sublayer velocity gradient in SPEC and the spatial resolution in SRCC.

						SPEC			SRCC		
Cases	Freq. (Hz)	p.p.p.	Snapshots	Tu_τ/δ	TU_∞/δ	$\Delta y^+_{\text{pixel}}$	N	$\varepsilon_{\frac{\partial \overline{U}}{\partial y}}$ (%)	IW	$\Delta x^+ \times \Delta y^+$	$\varepsilon_{\frac{\partial \overline{U}}{\partial y}}$ (%)
WT1	125	0.0058	27280	1.16	24.2	0.03	83	0.58	512 × 2	17 × 0.06	0.07
WT2	250	0.0043	49104	1.97	47.9	0.07	35	0.54	512 × 2	35 × 0.14	0.18
WT3	500	0.0047	70928	3.26	81.7	0.10	25	0.55	512 × 2	51 × 0.20	0.62
WT4	500	0.0025	92752	3.91	101.4	0.12	21	0.70	512 × 4	62 × 0.48	0.17
WT5	1000	0.0032	109120	6.72	182.1	0.22	12	1.59	512 × 4	110 × 0.86	1.41
WC1	800	0.0035	130956	4.94	99.2	0.03	83	0.95	512 × 4	15 × 0.12	0.32
WC2	1125	0.0033	130956	4.46	103.4	0.06	45	0.82	512 × 4	28 × 0.22	0.42
WC3	1600	0.0017	130956	5.28	132.6	0.09	26	0.61	512 × 4	48 × 0.38	0.10
WC4	3000	0.0014	246528	9.24	236.6	0.14	17	3.47	512 × 4	73 × 0.57	0.66

were recorded by high-speed CMOS cameras (Photron FastcamSA2/86K-M3) through macro lens (TAMRON SP AF 180 mm F/3.5 MACRO1:1). For WT1 ∼ WT5, one CMOS camera with full-frame resolution of 2048×2048 pixels was used. The field of view (FOV) was about 36.8 × 36.8 mm^2 (streamwise span× spanwise span) and the corresponding optical magnification varied from 0.03 to 0.22 wall units/pixel with the increase of Re_τ. The CMOS camera has an internal memory of 32 GB, enabling one continuous sampling of 5456 images at full-frame resolution. For WCs, two synchronized CMOS cameras were positioned along the streamwise direction with a gap of 0.12 m for the purpose of investigating the convection speed of WSS at large streamwise gap (to be discussed in Sec. IV B). To increase the time duration of one continuous sampling, cameras in WCs were operated at half-frame mode (with resolution of 1024×2048 pixels). The FOV was about 10.8 × 21.6 mm^2 for each camera and the magnification was 0.03 ∼ 0.14 wall units/pixel. The image sampling frequency, as summarized in Table III, was determined based on the principle that the maximum particle offset between two straddle images was no more than 12 pixel. For each case, at least five repetitions of continuous sampling were taken, resulting in an ensemble of $2 \times 10^4 \sim 2 \times 10^5$ snapshots or an eddy turnover time of $Tu_\tau/\delta = 1.16 \sim 9.24$ (or $TU_\infty/\delta = 24.2 \sim 236.6$). Note that such a limited sampling duration is attributed to the continuous recording mode that requires large storage capability. But the convergence of the first two-order statistics can be guaranteed even at the highest Re_τ case.

Two of the practical limitations for the near-wall PIV measurement are the wall reflection and the sparsity of the particles. Note that both the flat plate in WTs and the bottom wall in WCs are made of hydraulic-smooth glass. With a perpendicular light incident (as illustrated in Fig. 1), wall reflection that contaminates those particles very close to wall is rather weak, as can be seen in Fig. 5(a). In this sense, there is no necessary to perform a background subtraction before velocity-field calculation. As for the second issue, no additional tracer particles were released from the wall to avoid any disturbance to bias the near-wall flow. Therefore, the number of particles per pixel (p.p.p.) below $y^+ = 30$, as summarized in Table III, are quite smaller than the commonly accepted value that will yield discernible cross-correlation peak in a conventional WC algorithm [60]. For a compensation, the effective size of IW in SRCC will be enlarged to accommodate sufficient optical information. This will be further described later.

B. Mean WSS estimation via SPEC

Recalling that estimating WSS requires high spatial resolution of velocity fields in the near-wall region. The most suitable solution, to our knowledge, is to perform PTV. But three practical issues constraint its application for this purpose. First, owing to the relatively long exposure time that is

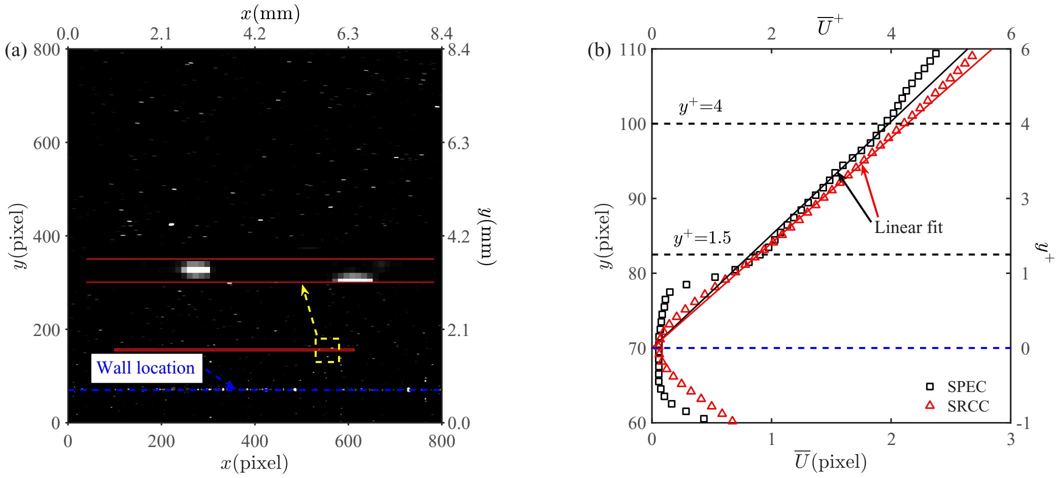

FIG. 5. (a) An example of the near-wall part of one snapshot of particle image in WC4, the red rectangle indicates one IW in the SRCC method. The inset is an enlarged plot of the yellow box. The blue dashed line indicates the wall location to show the mild wall reflection. (b) Comparison of $\overline{U}(y)$ in WC4 calculated by the SPEC and SRCC method, the solid lines indicate the linear fitting of $\overline{U}(y)$ in the range of $1.5 < y^+ < 4$.

constrained by the sampling frequency of CMOS cameras, individual particle images suffer distinct elongation along the convection direction. This can be seen from the zoomed-in plot in Fig. 5(a). It introduces additional uncertainty to the identification of the centroids of tracer particles. Second, the sparsity of tracer particles requires proper spatial average to yield a continuous near-wall velocity profile for the estimation of instantaneous velocity gradient, which is essentially the same as that embedded in SRCC. Third, the ratio of outliers in PTV due to particle mismatching is usually higher than that in WC-based PIV. Therefore, additional criteria for outlier detection and compensation is needed. In the SPEC or SRCC, since sufficient optical information is contained in one IW (to be presented later), outliers are rare and can be easily identified. Indeed, PTV was performed for Case WT4. It was found that the yielded mean velocity profile is consistent with the SRCC result beyond $y^+ = 1.5$, but the turbulent fluctuation intensity is comparably higher (not shown her for simplicity). Based on these considerations, we use the variants of WC-based PIV, i.e., SPEC and SRCC, for image post-processing.

SPEC method was taken at first for a reliable estimation of the mean WSS. In SPEC, IW is reduced to 1×1 pixel. Reduced optical information in the spatial domain is then compensated by ensemble averaging the cross-correlation map along time, which typically needs an ensemble of thousands of image pairs for a distinct correlation peak with sufficient signal-to-noise ratio (SNR) [41,43,61,62].

Figure 5(b) illustrates the mean velocity profile $\overline{U}(y)$ in WC4 (with the lowest p.p.p.) obtained by SPEC. A remarkable deviation of $\overline{U}(y)$ from the sublayer linear law is observed below $y^+ = 1.5$ and beyond $y^+ = 4$. The former is due to the adhesion of tracer particles on the wall, which cause enhanced light refection. The slope $\partial\overline{U}/\partial y$ was then estimated by the data points within $1.5 < y^+ < 4$ via a least-squares linear fitting. The uncertainty in determining $\partial\overline{U}/\partial y$ is affected by four aspects: the wall-normal resolution, the uncertainty in the velocity measurement, the number of points N being used in the fitting [39] and the precision of the wall location y_0 [40]. In SPEC, the spatial resolution is at single pixel level, corresponding to $\Delta y^+_{\mathrm{pixel}} = 0.03 \sim 0.22$ (as summarized in Table III). Consequently, the date point number N in the region of $1.5 < y^+ < 4$ is always larger than 12, enough for the linear fitting [39]. The uncertainty of the velocity measurement in SPEC is reported to be $0.02 \sim 0.04$ pixel [43]. Finally, the wall position y_0 can be precisely determined as the valley of the mirrored velocity profile centering around the glass wall [shown in Fig. 5(b)] with an uncertainty of $\Delta y^{+}_{\text{pixel}}$ that can be neglected for a leading-order estimation [40]. According to Hutchins and Choi [39], the uncertainty $\varepsilon_{\frac{\partial \overline{U}}{\partial y}}$ of the mean velocity gradient in the viscous sublayer taking into account all these factors can be estimated as

$$\sigma_{\overline{U}} = \sqrt{\frac{\sum_{i=1}^{N}(\overline{U}_i - \hat{U})^2 - \frac{\partial \overline{U}}{\partial y}\sum_{i=1}^{N}(y_i - \hat{y})(\overline{U}_i - \hat{U})}{N-2}}, \tag{3a}$$

$$\sigma_{\frac{\partial \overline{U}}{\partial y}} = \frac{\sigma_{\overline{U}}}{\sqrt{\sum_{i=1}^{N}(y_i - \hat{y})^2}}, \tag{3b}$$

$$\varepsilon_{\frac{\partial \overline{U}}{\partial y}} = \sigma_{\frac{\partial \overline{U}}{\partial y}} \Big/ \frac{\partial \overline{U}}{\partial y}. \tag{3c}$$

In the above formulation, $\overline{U}_i$ and y_i are the mean velocity and its wall-normal position of the ith point ($i = 1, 2, ..., N$) within $1.5 < y^{+} < 4$, $\hat{U}$ and $\hat{y}$ are the averaged value of $\overline{U}_i$ and y_i among N data points. $\sigma_{\overline{U}}$ can be regarded as the standard deviation of the experimental $\overline{U}$ about the fitted results and $\sigma_{\frac{\partial \overline{U}}{\partial y}}$ is the standard deviation of the fitted $\partial \overline{U}/\partial y$. As summarized in Table III, $\varepsilon_{\frac{\partial \overline{U}}{\partial y}}$ depends largely on the data point number N being used for the least-square fitting, which is in turn determined by the spatial resolution $\Delta y^{+}_{\text{pixel}}$. Except for case WC4 which has the smallest N, other cases have $\varepsilon_{\frac{\partial \overline{U}}{\partial y}}$ smaller than 1.0%, comparable to the typical uncertainty via single-point HWA measurement [39]. Finally, mean WSS is estimated by approximating $\partial \overline{U}/\partial y$ within $1.5 < y^{+} < 4$ to that at the wall.

C. Instantaneous WSS estimation via SRCC

The method of SRCC was used to get instantaneous velocity profile $U(y)$ in the near-wall region for the estimation of instantaneous WSS. The basic idea of SRCC is rather simple: the square-shaped IW in WC is replaced by a strip with wall-normal height significantly smaller than the streamwise length to enhance the resolution in former dimension [31,42]. Since the cross-correlation calculation and the correlation peak searching is unchanged, the basic principle in WC algorithm, i.e., one IW should contain sufficient optical information, need to be obeyed too. Willert [31] used a single row of 256×1 pixels as the IW, which is equivalent to a squared IW with a size of 16×16 pixels in terms of the amount of effective optical information being contained. In the present studies, the size of the strip-shaped IW was relaxed to 512×2 pixels in WT1 ∼WT3 or 512×4 pixels in the rest cases depending on their different p.p.p. in the near-wall region. This of course reduces the wall-normal resolution, but is a necessary compromise to guarantee that more than three particle images are equivalently contained in one IW. Combining with the relatively large diameters of particle images (5 ∼ 7 pixels) due to high magnification (11 ∼ 18 μm/pixel), this IW is enough to yield a distinct correlation peak with sufficient SNR.

A more critical issue in SRCC is that it sacrifices the streamwise resolution, so that the yielded $U(y)$ (and the estimated τ_w) is actually an average over a large streamwise span, i.e., $\Delta\tilde{x} = 512$ pixels or $\Delta\tilde{x}^{+} = 17 \sim 110$. In Sec. III D, it will be shown that such a streamwise average will only smooth out small-scale fluctuations whose streamwise length scales are smaller than $\Delta\tilde{x}$, but leave minor impact on both the statistics of WSS and its multiscale characteristics.

Instantaneous WSS, i.e., τ_w, is then estimated from the instantaneous $\partial U/\partial y$ in the linear range of the $U(y)$ profile. Note that Zhou and Xia [63] has shown that in a Rayleigh-Bernard turbulent convection flow, the upper bound of instantaneous viscous sublayer varies along time. A similar unsteadiness of the viscous sublayer in TBL is also observed here. To take into account this aspect, an iterative fitting method is proposed. The basic principle is to identify the well-behaved linear region of $U(y)$ by iteratively knocking out data points with large departure from the linear law. Figure 6 illustrates the procedure of this method. For any data point (U_i, y_i) in the range of $0 <$

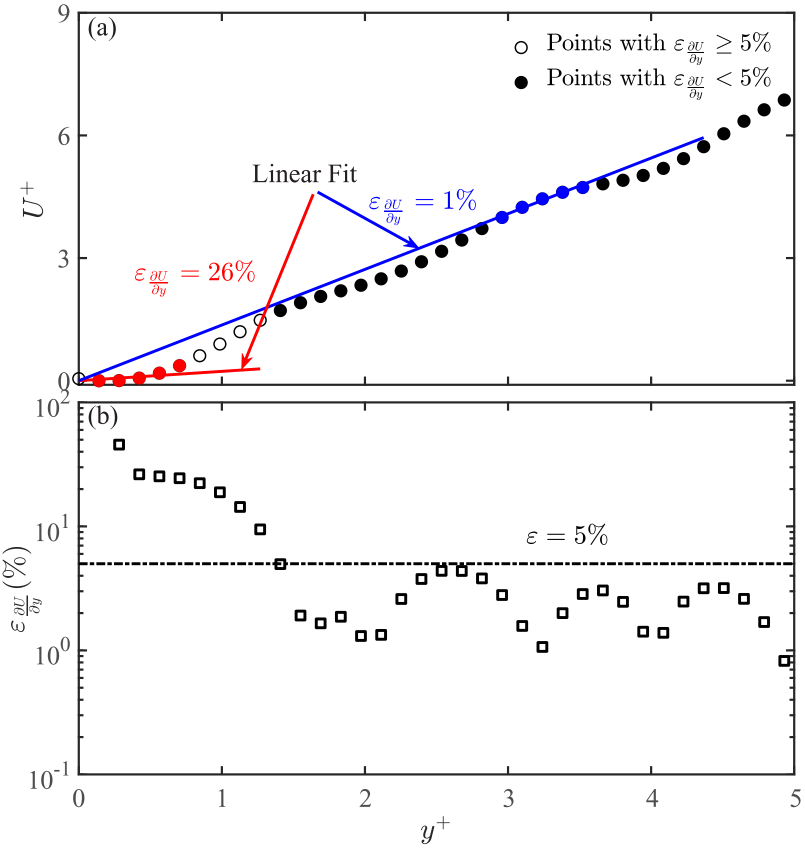

FIG. 6. (a) One profile of instantaneous $U^+(y^+)$ in WC4 being obtained by SRCC, the red and blue lines indicate a linear fitting of the subgroup of the red and blue data points, respectively. (b) Velocity gradient uncertainty $\varepsilon_{\frac{\partial U}{\partial y}}$ of each subgroup fitting.

$y^+ < 5$, a linear fitting is performed on its subgroup that covers at least four neighboring data points centering around it [see Fig. 6(a), for example]. The wall position y_0, that is obtained by SPEC in Sec. III B, is fixed for each fitting, and the velocity gradient uncertainty $\varepsilon_{\frac{\partial U}{\partial y}}$ at each (U_i, y_i) is estimated via Eq. (3) by replacing $\overline{U}$ with U. As illustrated in Fig. 6(b), $\varepsilon_{\frac{\partial U}{\partial y}}$ of all the examined data points scatter in a wide range (0.1% ∼ 50% below $y^+ = 5$), the large uncertainty below $y^+ = 1.5$ is caused by the particle adhesion effect, as has been seen in the $\overline{U}(y)$ profile obtained by SPEC [shown in Fig. 5(b)]. A tolerance of $\varepsilon_{\frac{\partial U}{\partial y}}$=5% is manually defined to knock out these data points with large deviation. Such a procedure iterates till no more outlier data point is removed. $\partial U/\partial y$ is finally obtained by performing a linear fitting to the left data points.

The feasibility of using SRCC and iterative fitting to estimate τ_w can be empirically evidenced by two aspects. First, as illustrated in Fig. 5(b) for WC4 (with the lowest p.p.p.), SRCC systematically overestimate $\overline{U}$ (and $\overline{\tau_w}$) if compared to SPEC. This is attributed to the reduced resolution in SRCC due to the enlarged size of IW in both two directions. Nevertheless, as summarized in Table IV, the relative differences between the estimated mean skin friction coefficients ($c_f = \frac{2\nu}{\rho U_\infty^2}\frac{\partial \overline{U}}{\partial y}|_{\text{linear}}$), i.e., $\epsilon_{c_f} = (c_f^{\text{SRCC}} - c_f^{\text{SPEC}})/c_f^{\text{SPEC}}$, are about 5% ∼ 7% in all the cases excluding WC2. Furthermore, the uncertainties of the mean velocity gradient obtained by SRCC, as estimated by Eq. (3), are lower than 1.6% (shown in Table III), comparable to those of the SPEC results. Second, Fig. 7 compares

TABLE IV. Mean skin friction coefficients obtained by SPEC and SRCC and their relative differences.

Cases	WT1	WT2	WT3	WT4	WT5	WC1	WC2	WC3	WC4
$10^3c_f^{\mathrm{SPEC}}$	3.79	3.29	2.77	2.65	2.51	3.03	3.64	3.10	2.99
$10^3c_f^{\mathrm{SRCC}}$	3.99	3.51	2.96	2.84	2.67	3.21	3.52	3.32	3.16
ϵ_{c_f}	5.3%	6.7%	6.9%	7.2%	6.4%	5.9%	−3.2%	7.3%	5.5%

two typical signals of WSS in WC4 and DNS4 at similar Re_τ, in which the time-series signal of $\tau_w(t)$ in WC4 is converted to a spatial signal $\tau_w(x)$ via Taylor frozen hypothesis with the convection speed being set to $u_c^+ = 12$ (to be discussed in Sec. IV B). Both two signals are characterized as a wide spectrum of scales with equivalent amplitudes. The difference is that due to the spatial averaging effect of SRCC, less small-scale fluctuations are presented in WC4. Besides, positive spikes of τ_w, which are attributed to the splattering of strong Q4 quadrant events [64], frequently appear in both cases. Spectrum analysis (to be presented in the following) will show that two signals have equivalent spectral characteristics.

D. Bias from the streamwise-average effect in SRCC

Recalling that SRCC achieves high resolution in the wall-normal direction at a price of relaxing the streamwise resolution. To quantify the effect of the enlarged width of IW on the statistics of the yielded WSS, a synthetic test on the DNS datasets was taken by moving averaging the signal of $\tau_w(x)$ along x direction:

$$\widetilde{\tau_w}(x, \Delta\widetilde{x}) = \frac{1}{\Delta\tilde{x}}\int_{x-1/2\Delta\tilde{x}}^{x+1/2\Delta\tilde{x}} \tau_w(x')dx'. \tag{4}$$

As illustrated in Fig. 7, $\Delta\tilde{x}$ is the width of the moving-average window to simulate the width of IW in the experiment cases. The resulted bias of the statistics of τ_w is defined as

$$\epsilon(F) = \frac{F(\widetilde{\tau_w}) - F(\tau_w)}{F(\tau_w)}, \tag{5}$$

where the function F indicates the first three-order moments of WSS. The relation of $\epsilon \sim \Delta\tilde{x}^+$ in all the DNS cases are shown in Fig. 8, in which the shaded region indicates the range of $\Delta\tilde{x}^+$ that correspond to the width of the IWs in the experiment cases. The bias of streamwise average on the mean WSS is considerably low even when $\Delta\tilde{x}^+ = 200$. With the level of $\epsilon(\overline{\tau_w}) \sim O(10^{-4})$, no distinct Re-dependency can be claimed. On the contrary, the magnitudes of σ_{τ_w} and S_{τ_w} decrease

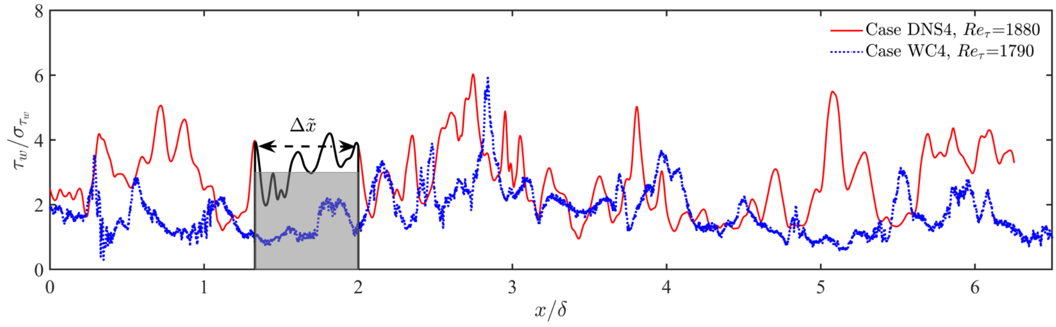

FIG. 7. Comparison of $\tau_w(x)$ in WC4 and DNS4 at similar Re_τ. The shaded region illustrates a window for moving average with a width of $\Delta\tilde{x}$.

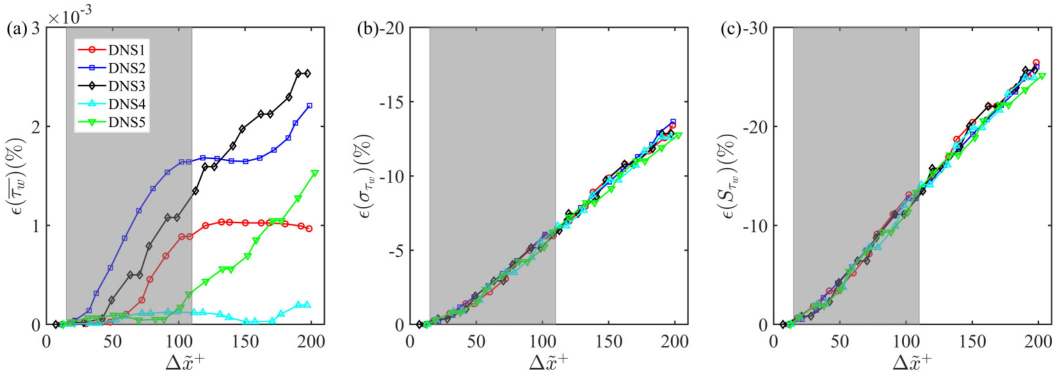

FIG. 8. Bias of (a) the mean value $\overline{\tau_w}$, (b) the RMS value σ_{τ_w} and (c) the skewness S_{τ_w} of WSS as a function of the width of the moving average window $\Delta\tilde{x}^+$. The shaded region indicates the range of the width of IWs in the experiment cases.

with the increase of $\Delta\tilde{x}$, the reduction level is quasilinearly proportional to $\Delta\tilde{x}$ without discernible Re-dependency. Given a range of $\Delta\tilde{x}^+ = 17 \sim 110$ ($\Delta\tilde{x}$=512 pix in the image plane) in the experiment cases, the reduction of σ_{τ_w} and S_{τ_w} are 0.2% $\sim$ 6.5% and 0.5% $\sim$ 14.1%, respectively. For the cases in the same group, the higher Re_τ (and $\Delta\tilde{x}^+$), the larger streamwise-average effect on the second- and third-order moments.

Figure 9 reveals the effect of $\Delta\tilde{x}$ on both the PDF and the premultiplied energy spectrum of τ_w'. Since all the DNS cases present similar results, only those of DNS5 are presented for simplicity. As shown in Fig. 9(a), only the PDFs of the extreme τ_w' events are affected by $\Delta\tilde{x}$. This observation can be attributed to the smear out of the peaks and valleys of $\tau_w'(x)$ due to the moving average operation. It well explains the decrease of σ_{τ_w} and S_{τ_w} with the increase of $\Delta\tilde{x}$ (shown in Fig. 8). Fluctuations with streamwise length smaller than the window width will be also wiped out by the moving average operation, leading to the suppression of the energy content of small scales, which is evident from the premultiplied streamwise energy spectrum $k_x\phi_{\tau_w'\tau_w'}(\lambda_x)$ shown in Fig. 9(b). Nevertheless, the

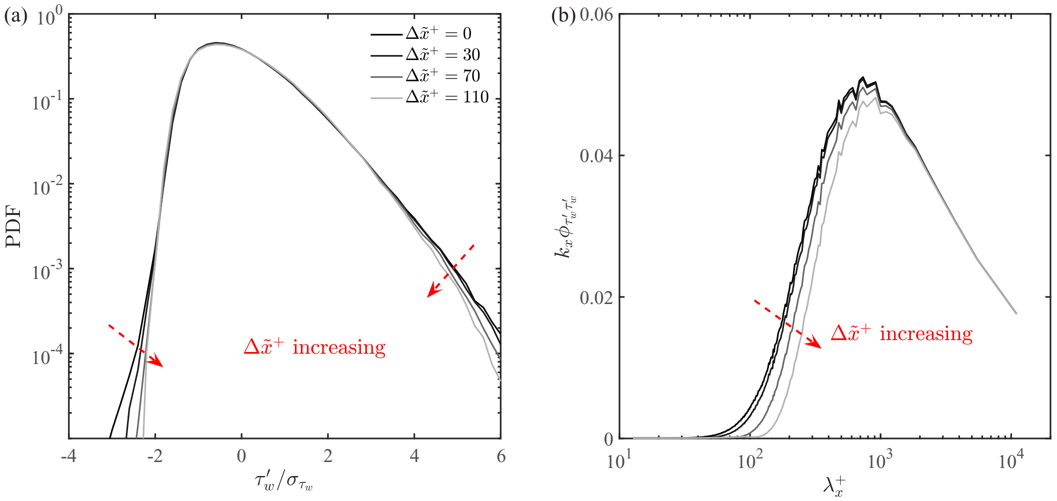

FIG. 9. Effect of the streamwise moving average on (a) the PDF and (b) the premultiplied energy spectrum of τ_w' in DNS5.

large-scale part (with $\lambda_x^+ > 1000$) remains unaffected, so does the wavelength of the energy spectra peak $\lambda_{x,\max}$.

To sum up, the comparably large width of the IW in SRCC serves as a high-pass filter to smear out small-scale high-magnitude fluctuations in τ_w'. Despite of the bias in the statistics, it has limited impact on the PDF and the energy spectrum. It is stressed that the main limitation of this method is that WSS fluctuations with streamwise length smaller than the IW width ($17 \sim 110$ wall units in the present experimental cases) can not be resolved. For example, the occurrence probability of negative τ_w events has been examined to be $O(10^{-4})$ in DNS cases. But no backward flow in the vicinity of the wall has been observed in experiment cases. The reason is that the typical streamwise length of these extreme events, i.e., 20 ∼30 wall units [21,65,66], are smaller than the present IW width. Despite of this limitation, it is argued that the spectrum analysis shown in Fig. 9(b) indicates that the scales with $\lambda_x^+ < 110$ only contribute a small portion of the energy of WSS. The absence of these small-scales would not affect the following observation on the multiscale characteristics of WSS qualitatively. The synthetic test taken here will also provide a reference for estimating the uncertainty of the statistics of WSS in the experiment cases.

IV. Re-DEPENDENCY OF THE STATISTICS OF WSS

Using both the experimental and the DNS datasets, the characteristics of the WSS, as well as its Re-dependency, will be examined. This section deals with the high-order moments and the PDFs of WSS. To facilitate the spectral analysis in the next section, its mean convection speed is also analyzed here.

A. Statistics of WSS

The mean skin friction coefficients of all the experiment cases obtained by SRCC are shown in Fig. 10(a). Except for WC1 where the low Re effect is remarkable, a collapse to the semiempirical correlation, i.e., $c_f = 2(1/\kappa \ln \mathrm{Re}_\theta + 4.127)^{-2}$ [6], is seen with relative differences smaller than 7%. Note that such a difference is mild if compared to previous measurements [denoted as black symbols in Fig. 10(a)]. Figures 10(b) and 10(c) compare the RMS and the skewness of τ_w' to the existing data. The error bars indicate the bias introduced by the streamwise average embedded in the SRCC algorithm, which are estimated by the synthetic test on the DNS datasets being taken in Sec. III D. Except for WC1, $\sigma_{\tau_w}^+$ of all the experiment cases are seen to well follow the logarithmic correlation of $\sigma_{\tau_w}^+ = 0.298 + 0.018 \ln \mathrm{Re}_\tau$ [22,28] with relative differences smaller than 5%. Meanwhile, the DNS cases seem to systematically underestimate $\sigma_{\tau_w}^+$ by about 6%, but the logarithmic scaling still works. As for the skewness, all the present cases scatter around a constant value of $S_{\tau_w} = 1$ without clear Re-dependency. The scattering is mild if compared to the existing data (black symbols in Fig. 10(c)). Note that there are two exceptions, i.e., WT3 and WC3 with similar Re_τ, which have considerably larger deviation from $S_{\tau_w} = 1$ but with different signs. This, to our knowledge, highlights the difficulty in achieving a convergence state for the third-order moments.

Figure 11 summarizes the PDFs of the fluctuating WSS normalized by its RMS value, i.e., $\mathrm{PDF}(\tau_w'/\sigma_{\tau_w})$. One of the PDF profiles in Ref. [26] with the highest Re number ($\mathrm{Re}_\tau = 625$) is also included for a comparison. For all the present studied cases, a good collapse of $\mathrm{PDF}(\tau_w'/\sigma_{\tau_w})$ is observed in the range of $-2 < \tau_w'/\sigma_{\tau_w} < 3$. With the increase of Re_τ, the hierarchical lowering of the probability of extreme events outside this range is evident in the experiment cases. This is attributed not to the Re-dependency but to the streamwise average effect embedded in SRCC, as has been demonstrated in Fig. 9. Diaz-Daniel *et al.* [26] reported a slow increase of the probability of extreme τ_w' events in $\mathrm{Re}_\tau = 409 \sim 625$. Such a trend also appears in DNS1∼DNS3 with $\mathrm{Re}_\tau < 1300$. Nevertheless, a clear Re-dependency is absent in DNS3∼DNS5 with higher Re_τ. This, to our knowledge, is consistent with the assumption of a constant skewness ($S_{\tau_w} = 1$). It is further noted that despite of a similar Re_τ, the profile of DNS1 in the extreme-value side (with $\tau_w'/\sigma_{\tau_w} < -2$ or >3) fails to collapse to that in Ref. [26]. Such a difference reminds us that extreme WSS events

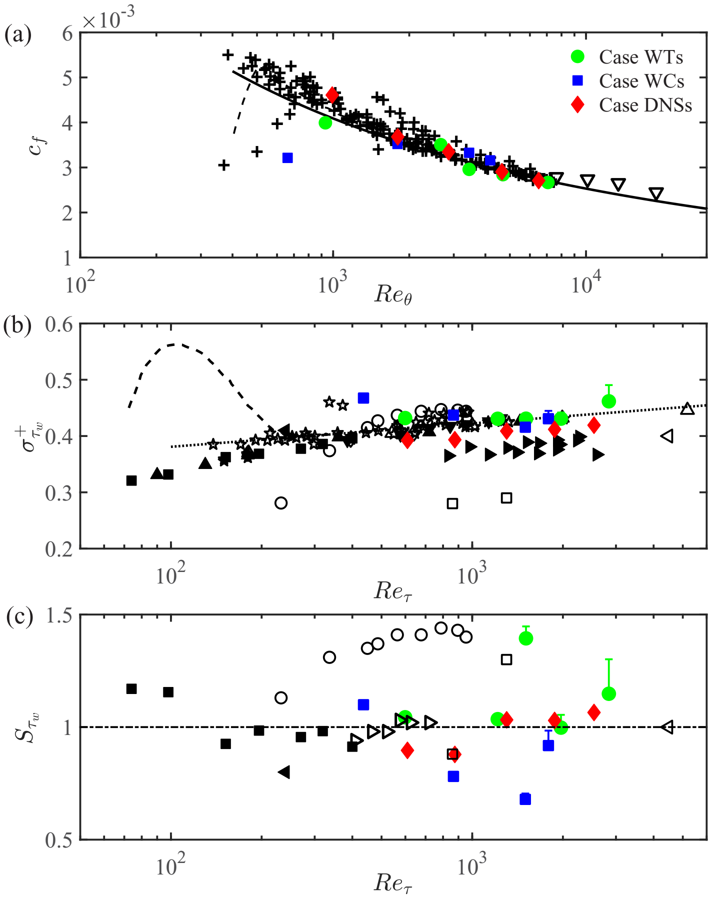

FIG. 10. Re-dependency of (a) the skin friction coefficient, (b) the RMS value and (c) the skewness of τ'_w. In (a), the solid line indicate the empirical relation of $c_f = 2(1/\kappa \ln \mathrm{Re}_\theta + 4.127)^{-2}$ [6], + indicates results being summarized in Ref. [50], ▽ indicates results obtained in Ref. [67]. In (b), the dotted line represents $\sigma^+_{\tau_w} = 0.298 + 0.018 \ln \mathrm{Re}_\tau$; the dashed line indicates the results in Ref. [26]. Black markers in (b) and (c) represent data from literatures listed in Table I.

might be rather sensitive to the configuration of the simulation, i.e., the triggering or inflow/outflow condition. Based on this observation, whether a "universal" PDF distribution of the fluctuating WSS can be expected in high Re scenario is still an open question.

B. Convection speed of WSS

Owing to the time-resolved feature of the present measurement, it is possible to study the multiscale characteristics of the time-series signal of $\tau'_w(t)$ via spectral analysis. To keep consistency with the DNS cases, in which $\tau'_w(x)$ is extracted from each snapshot, $\tau'_w(t)$ in the experiment ones needs to be converted to spatial signal via Taylor's frozen hypothesis with a convection speed u_c.

The determination of the convection speed is an important issue, since Yang and Howland [68] recently found that the improper selection of the convection speed of large-scale turbulent fluctuations will bias the magnitude of the amplitude modulation coefficient. Both Del Álamo and Jiménez [69] and Monty and Chong [70] showed that the convection speed of near-wall turbulent fluctuation was scale dependent. Namely, large-scale components in the inner layer, which can be regarded as the footprints of outer-layer LSMs/VLSMs, have convection speed larger than the mean

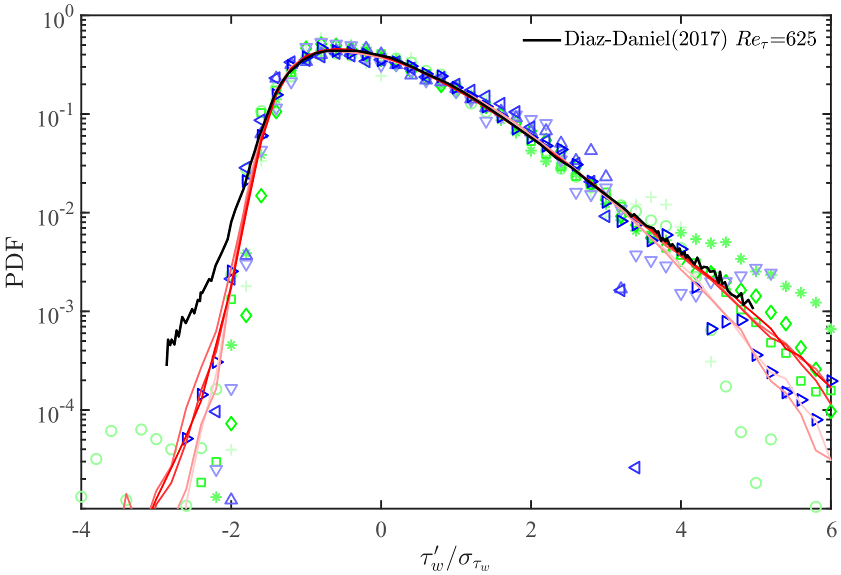

FIG. 11. PDFs of τ'_w normalized by σ_{τ_w}. Symbol list is given in Table II.

velocity at the same flow layer, while small-scale ones were expected to convect downstream at a speed of $u_c^+ = 11$. Jeon *et al.* [71] and Hutchins *et al.* [27] both showed that the convection speed of WSS presents a similar scale dependency. However, Diaz-Daniel *et al.* [26] determined $u_c^+ = 11$ as the averaged convection speed of all the wavenumber components of WSS in low Re scenario, and reported a strong dependency of u_c/U_∞ on Re_τ. Liu *et al.* [21] recently measured instantaneous WSS by an array of streamwise-aligned micro-pillar sensors. They found that u_c/U_∞ of WSS decreased from 0.53 at $\mathrm{Re}_\tau = 860$ to 0.46 at $\mathrm{Re}_\tau = 1300$.

Here, the mean convection speed of WSS is obtained by the conventional two-point correlation methods, similar to Refs. [21,26,27]. In WTs, multiple single-point signals of $\tau_w(t)$ can be sampled at various x stations within the streamwise FOV of one camera (2048 pix), which accommodates a gap of $\Delta X/\delta \approx 0.02 \sim 0.1$ between two sampling stations. However, the configuration of two streamwise-aligned cameras in WCs increases the maximum gap to $\Delta X/\delta \approx 0.9$.

Figures 12(a) and 12(b) illustrate the time-shifted signals $\tau'_w(t + \Delta t_{\max})$ at different x stations in WT5 and WC4, respectively. $\Delta t_{\max}$ is the time lag between $\tau'_w(x, t)$ and $\tau'_w(x + \Delta X, t)$ at which the time-lag correlation coefficient, being defined as

$$R_{\tau'_w(x)\tau'_w(x+\Delta X)}(\Delta t) = \frac{\overline{\tau'_w(x,t)\tau'_w(x+\Delta X, t+\Delta t)}}{\sigma_{\tau'_w(x,t)}\sigma_{\tau'_w(x+\Delta X,t+\Delta t)}}, \tag{6}$$

reaches maximum. Such a time-shifted plot shows that the resemblance between $\tau'_w(x, t)$ and $\tau'_w(x + \Delta X, t + \Delta t)$ significantly relaxes as ΔX increasing from 0.1δ to 0.9δ. Nevertheless, the curve of $R_{\tau'_w(x)\tau'_w(x+\Delta X)} \sim \Delta t$ still presents a detectable correlation peak (at $\Delta t_{\max}$) even with $\Delta X = 0.9\delta$ [shown in Fig. 12(d)]. This can be attributed to the contribution from those large-scale fluctuations whose life span are comparably long. Figures 12(e) and 12(f) plot $\Delta t_{\max}$ as a function of ΔX in the cases of WTs and WCs, respectively. A linear correlation, i.e., $\Delta t_{\max} \propto \Delta X$, is always presented when $\Delta X \leqslant 0.9\delta$. The slope $\Delta X/\Delta t_{\max}$ is then used to approximate the mean convection speed $\overline{u_c}$ averaged among all the resolved scales. Recalling that Hutchins *et al.* [27] found that in high Re scenario ($\mathrm{Re}_\tau = 14150$), u_c of WSS obtained at large ΔX was higher than that at small ΔX due to the footprint of LSMs/VLSMs in the outer layer. In the next section, it will be shown that the footprint effect is not significant in the present cases with comparably lower Re_τ. Therefore, $\overline{u_c}$ is

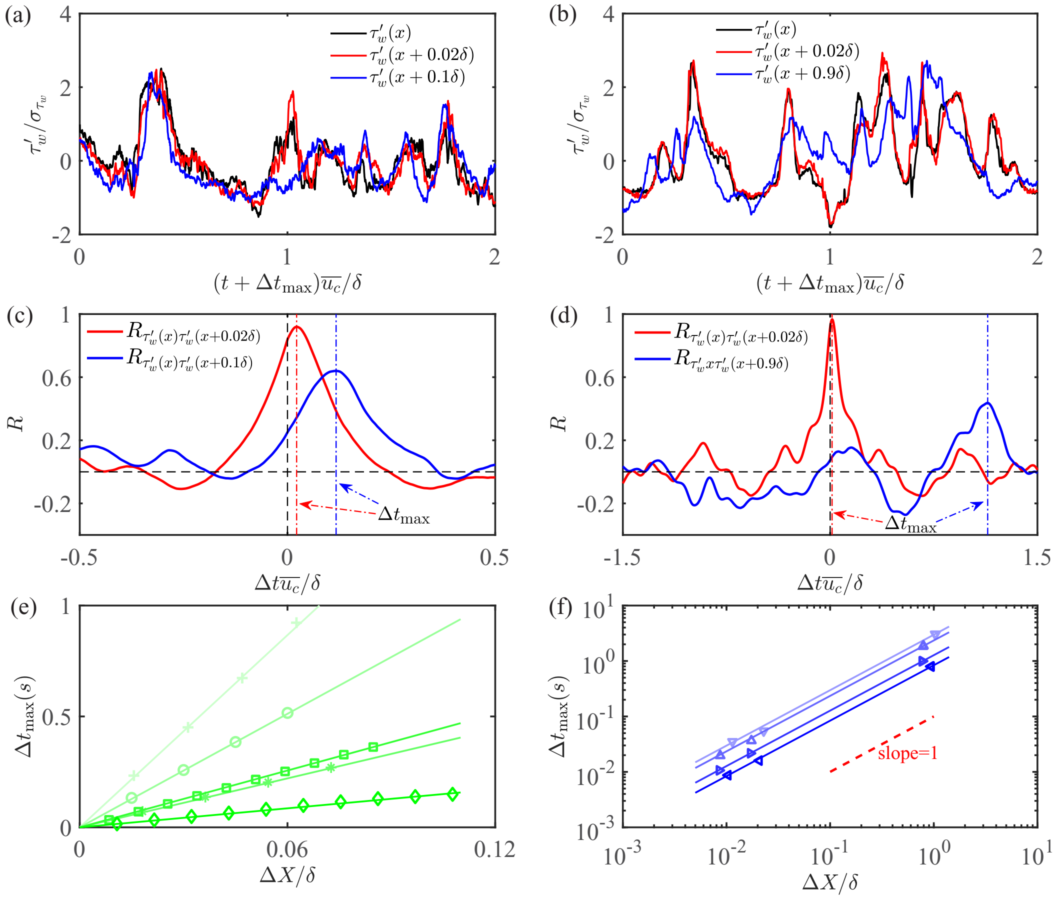

FIG. 12. (a, b) Time-shifted signals of τ'_w at various x stations in WT5 or WC4; (c, d) time-lag correlations of the signals shown in (a, b); (e, f) $\Delta t_{\max}$ as a function of ΔX in the cases of WTs or WCs. The solid lines in (e, f) indicate linear fitting and the red dashed line in (f) has a slope of 1 in the log-log axes.

used for the space-time conversion. It is noted that the ignorance of the disparity of convection speed among different scales will not qualitatively affect the spectral analysis to be discussed in the next section.

Figure 13 summarizes $\overline{u_c}$ of all the experiment cases in either inner scaling or outer scaling. The inner-scaled results scatter around $\overline{u_c}^+ = 12$ with the deviation lower than 13% [see Fig. 13(a)]. Note that $\overline{u_c}^+ = 12$, instead of $\overline{u_c}^+ = 11$ that has been reported in previous literatures [26,69,70], is set as the baseline. The reason might be the streamwise averaging effect of the SRCC algorithm, which reduces the weight of the contribution of small-scale fluctuations to $\overline{u_c}$. The outer-scaled $\overline{u_c}/U_\infty$, however, presents a distinct Re-dependency, consistent with the observation of Diaz-Daniel *et al.* [26] in lower Re regime. Given a fixed value of $\overline{u_c}^+ = 12$ and the semiempirical formulation of $U_\infty/u_\tau \sim \mathrm{Re}_{\delta^*}$ in Eq. (2) [59], the following correlation can be expected:

$$\overline{u_c}/U_\infty = 4.61/(\ln \mathrm{Re}_{\delta^*} + 1.27). \quad (7)$$

As a comparison, the correlation of $\overline{u_c}/U_\infty = 4.22/(\ln \mathrm{Re}_{\delta^*} + 1.27)$ with $\overline{u_c}^+ = 11$ is also shown in Fig. 13(b). These two curves clap the experiment data in the between. Nevertheless, the logarithmic Re-dependence predicted by Eq. (7) is evidenced. In the following, we will use $\overline{u_c}^+ = 12$ as the leading-order estimation of the mean convection speed of instantaneous WSS.

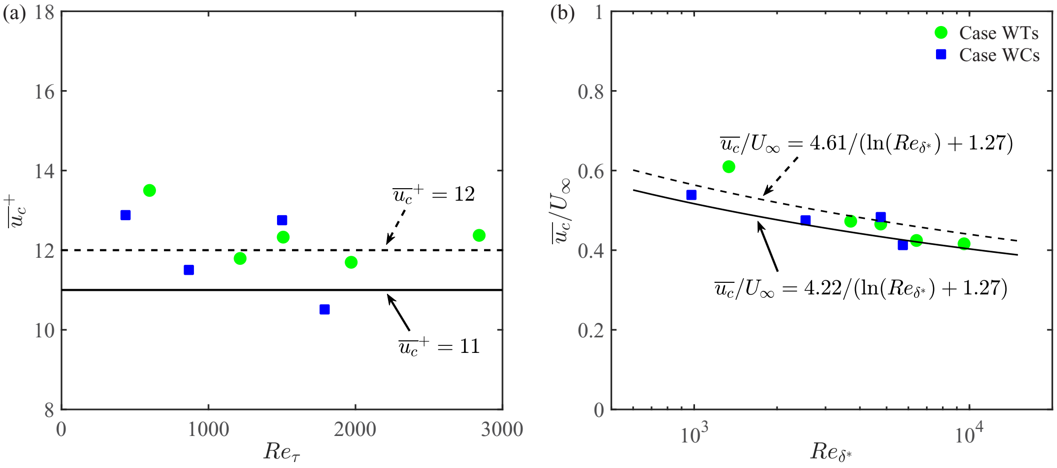

FIG. 13. Re-dependency of the mean convection speed of τ_w' normalized by (a) u_τ and (b) U_∞.

However, on considering the footprint effect of LSMs/VLSMs, it is unclear whether such a constant convection speed works in high Re regime.

V. MULTISCALE CHARACTERISTICS OF WSS

In this section, the multiscale characteristics of WSS is to be studied by spectral analysis. The temporal signals $\tau_w'(t)$ in the experiment cases are converted to spatial signals $\tau_w'(x)$ with convection speed $\overline{u_c}$ being estimated in Sec. IV B. It is noted that the mild uncertainty in $\overline{u_c}$ will not qualitatively affect the following observation on the energetic length scale of WSS and its scaling behavior.

A. Spectra analysis

Figure 14 shows all the premultiplied streamwise energy spectra $k_x\phi_{\tau_w'\tau_w'}(\lambda_x)$ of WSS. Three kinds of scalings for λ_x, i.e., the inner scaling by l^*, the mixed scaling by $(l^*\delta)^{1/2}$ and the outer scaling by δ, are tested. All the spectra are normalized by their peak values. The spectrum with $\mathrm{Re}_\tau = 625$ in Ref. [26] is also included for comparison. Comparing to the other two ones, the

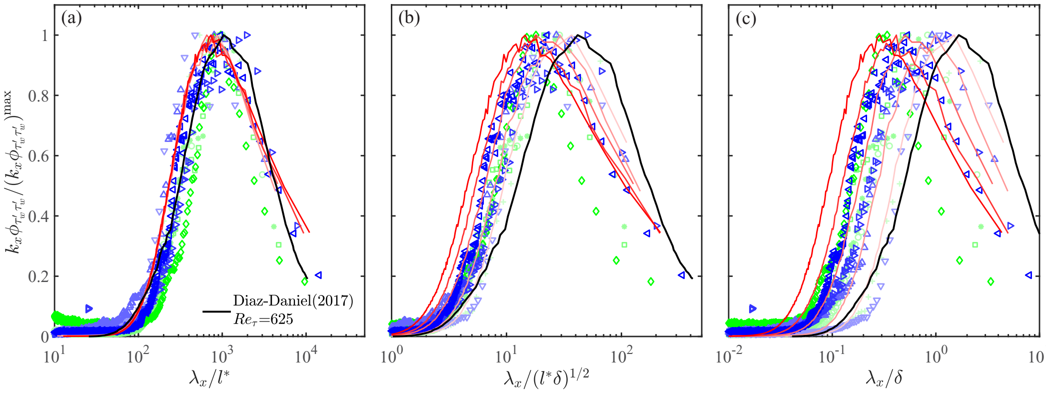

FIG. 14. Premultiplied streamwise energy spectra of τ_w'. $k_x\phi_{\tau_w'\tau_w'}$ are normalized by their peak values, the wavelength λ_x are normalized by (a) l^*; (b) $(l^*\delta)^{1/2}$ and (c) δ. Symbol list is given in Table II.

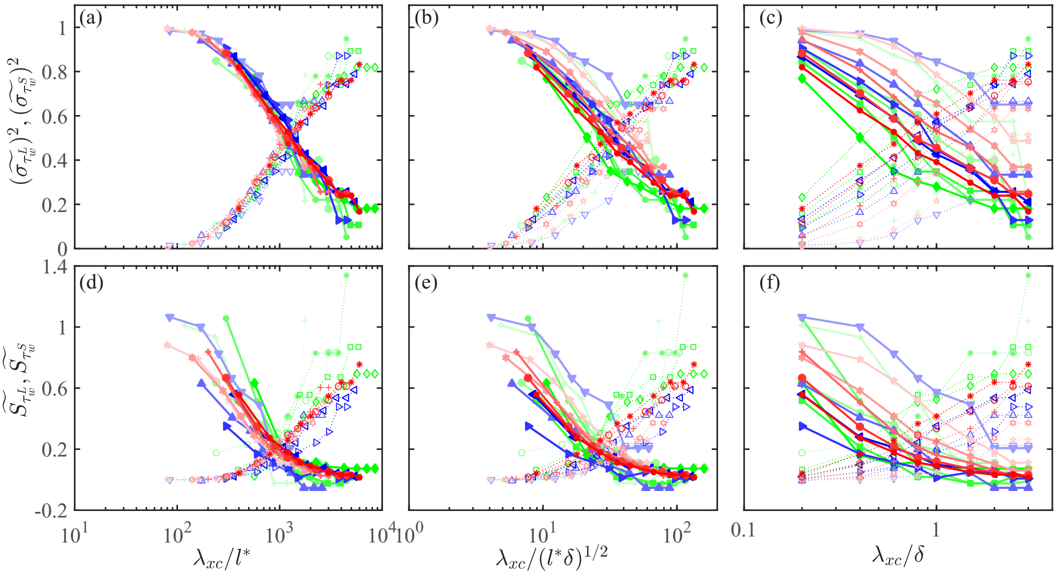

FIG. 15. The variance (a–c) and the skewness (d–f) of LS and SS as a function of λ_{xc} normalized by (a, d) l^*, (b, e) $(l^*\delta)^{1/2}$, and (c, f) δ in all the studied cases. Symbol list is given in Table II, filled symbols with solid lines indicate the LS components and hollow symbols with dotted lines indicate the SS ones.

inner scaling collapses the spectral curves with various Re_τ. This observation is consistent with Refs. [13,20] in low Re TBL or TCF. Furthermore, the spectral peak is always presented at $\lambda^+_{x\mathrm{peak}} \approx 1000$, comparable to the mean length of low-speed streaks in the buffer layer that are regarded to play a dominant role in generating WSS [26].

Recalling that Örlü and Schlatter [28] reported a Re-dependency of the inner-scaled WSS spectrum in a DNS TBL with $\mathrm{Re}_\theta = 1100 \sim 4000$. They attributed it to the enhanced contribution of the footprint of LSMs/VLSMs to WSS. However, the DNS of Diaz-Daniel *et al.* [26] with $\mathrm{Re}_\theta = 1090 \sim 1820$ did not reveal a distinct elevation of the large-scale part of the WSS spectrum, neither do the present analyzed DNS datasets (DNS1∼DNS5 with $\mathrm{Re}_\theta = 900 \sim 6500$). The lack of a distinct Re-dependency can be further evidenced by the experiment cases. Namely, in the same dataset group (Case WTs or WCs), the spectra on the right-hand side of $\lambda^+_{x\mathrm{peak}}$, which are less affected by the streamwise average effect, well collapse with each other. Note that difference in the spectra between two experiment groups is remarkable, but to our knowledge, this is due to the different experiment facility.

The observed Re-insensitivity of the WSS spectrum suggests a rather weak footprint effect in the present low-to-moderate Re range, since it infers an energy contribution of large-scale components that is quasi-invariant to Re (as will be shown later). A possible explanation is that for inviscid motions associated with LSMs/VLSMs in the outer layer, it is quite difficult for them to penetrate deep into the viscous dominated near-wall region; instead, they mainly affect small-scale turbulent motions there via the so-called amplitude modulation mechanisms [72,73]. This inference will be further inspected in the following from the aspect of scale decomposition.

B. Scale decomposition of WSS

The signals of $\tau'_w(x)$ were decomposed into small-scale components τ'^S_w (denoted as SS) and large-scale ones τ'^L_w (denoted as LS) via sharp-edge filter at a pregiven cutting-off boundary λ_{xc}. Figure 15 plots the variance ($(\widetilde{\sigma_{\tau_w^L}})^2$ or $(\widetilde{\sigma_{\tau_w^S}})^2$) and the skewness ($\widetilde{S_{\tau_w^L}}$ or $\widetilde{S_{\tau_w^S}}$) of the LS or the SS components of WSS as a function of λ_{xc}, which is normalized by either l^*, $(l^*\delta)^{1/2}$ or δ. Note that the variance and the skewness of LS and SS are normalized by the variance of the original signals [$\overline{(\tau'_w)^2}$ or $(\overline{(\tau'_w)^2})^{3/2}$] instead of by their own values. This enables the following component decomposition, i.e.,

$$\frac{\overline{(\tau'_w)^2}}{\overline{(\tau'_w)^2}} = 1 = \frac{\overline{(\tau'^L_w + \tau'^S_w)^2}}{\overline{(\tau'_w)^2}} = \underbrace{\frac{\overline{(\tau'^L_w)^2}}{\overline{(\tau'_w)^2}}}_{(\widetilde{\sigma_{\tau^L_w}})^2} + \underbrace{\frac{\overline{(\tau'^S_w)^2}}{\overline{(\tau'_w)^2}}}_{(\widetilde{\sigma_{\tau^S_w}})^2} + \underbrace{\frac{\overline{(2\tau'^L_w\tau'^S_w)}}{\overline{(\tau'_w)^2}}}_{\text{cross term}}, \tag{8}$$

$$\begin{aligned} S_{\tau_w} \approx 1 = \frac{\overline{(\tau'_w)^3}}{\left(\overline{(\tau'_w)^2}\right)^{3/2}} = \frac{\overline{(\tau'^L_w + \tau'^S_w)^3}}{\left(\overline{(\tau'_w)^2}\right)^{3/2}} = \underbrace{\frac{\overline{(\tau'^L_w)^3}}{\left(\overline{(\tau'_w)^2}\right)^{3/2}}}_{\widetilde{S_{\tau^L_w}}} + \underbrace{\frac{\overline{(\tau'^S_w)^3}}{\left(\overline{(\tau'_w)^2}\right)^{3/2}}}_{\widetilde{S_{\tau^S_w}}} \\ + \underbrace{\frac{\overline{3(\tau'^L_w)^2\tau'^S_w}}{\left(\overline{(\tau'_w)^2}\right)^{3/2}}}_{\text{cross term I}} + \underbrace{\frac{\overline{3\tau'^L_w(\tau'^S_w)^2}}{\left(\overline{(\tau'_w)^2}\right)^{3/2}}}_{\text{cross term II}}, \end{aligned} \tag{9}$$

that suggests a counteracting contribution of LS and SS to the overall fluctuating energy of WSS and its skewness. An opposite λ_{xc}-dependency between $(\widetilde{\sigma_{\tau^L_w}})^2$ and $(\widetilde{\sigma_{\tau^S_w}})^2$, as well as $\widetilde{S_{\tau^L_w}}$ and $\widetilde{S_{\tau^S_w}}$, is clearly evident in Fig. 15. Decreasing λ_{xc} promotes the contribution of LS, since more scale components are grouped into large-scale domain. Comparing to the mixed or outer scaling, the inner scaling of λ_{xc} leads to a weak Re-dependency of the scale-decomposed variance and skewness. This accords well with the inner-scaling nature of the spectrum of WSS shown in Fig. 14.

Interestingly, the curves of $(\widetilde{\sigma_{\tau^L_w}})^2 \sim \lambda^+_{xc}$ are seen to intercept with those of $(\widetilde{\sigma_{\tau^S_w}})^2 \sim \lambda^+_{xc}$ around $\lambda^+_{xc} \approx 1000$ [in Fig. 15(a)], so do the curves of $\widetilde{S_{\tau^L_w}} \sim \lambda^+_{xc}$ and $\widetilde{S_{\tau^S_w}} \sim \lambda^+_{xc}$ [in Fig. 15(d)]. The variance and the skewness of LS/SS with $\lambda^+_{xc} = 1000$ are then plotted as a function of Re_τ in Figs. 16(a) and 16(c). As a comparison, Figs. 16(b) and 16(d) show the corresponding data with $\lambda_{xc}/\delta = 1$, which was widely used as the scale separation boundary when studying the amplitude modulation effect [72,74,75]. For $\lambda^+_{xc} = 1000$, the skewness of LS are comparable to those of SS, i.e., $\widetilde{S_{\tau^L_w}} \sim \widetilde{S_{\tau^S_w}}$, without discernible Re-dependency, while the ratios between their variance are quasi-invariant, i.e., $(\widetilde{\sigma_{\tau^L_w}})^2 : (\widetilde{\sigma_{\tau^S_w}})^2 \approx 3:2$. None of these observations are evident when $\lambda_c/\delta = 1$. Instead, the weighting between $(\widetilde{\sigma_{\tau^L_w}})^2$ and $(\widetilde{\sigma_{\tau^S_w}})^2$ (or $\widetilde{S_{\tau^L_w}}$ and $\widetilde{S_{\tau^S_w}}$) flips beyond $\mathrm{Re}_\tau \approx 1200$ (or $\mathrm{Re}_\tau \approx 700$), indicating the dominancy of SS to the fluctuating characteristics of WSS once Re_τ exceeding this value. Note that such a flipping is conflict to the conventional viewpoint that large-scale motions pose increasing contribution to flow-field turbulent fluctuations in high Re scenario. It is thus argued that $\lambda_{xc} \sim \delta$ is not a proper cutting-off boundary for the scale decomposition of WSS, at least in the present studied Re_τ range.

Finally, with the weak Re-dependency of $\widetilde{S_{\tau^L_w}}$ and $\widetilde{S_{\tau^S_w}}$ when using $\lambda^+_{xc} = 1000$ as the cutting-off boundary, the cross term II in Eq. (9), i.e., $X_{\mathrm{II}} \equiv \frac{\overline{3\tau'^L_w(\tau'^S_w)^2}}{(\overline{(\tau'_w)^2})^{3/2}}$, is expected to be insensitive to Re_τ. This conjecture relies on two additional conditions: S_{τ_w} is Re-independent and the cross term I is rather small [76]. Both are valid in the present studied Re_τ range. In the DNS cases, X_{II} (with $\lambda^+_{xc} = 1000$) varies in a mild range of $0.45 \sim 0.55$ without clear Re-dependency, but the scattering in the experiment cases is comparably large (in the range of $0.30 \sim 0.61$) due to both the insufficient resolution in the SS components and the difficulty in reaching statistical convergence. Whether an invariant X_{II} does exist, especially in higher Re scenario, is an interesting issue to be further studied in the future. The reason is that this cross term serves as an alternating measure of the amplitude modulation coefficient [77]. According to Marusic *et al.* [78], the near-wall velocity

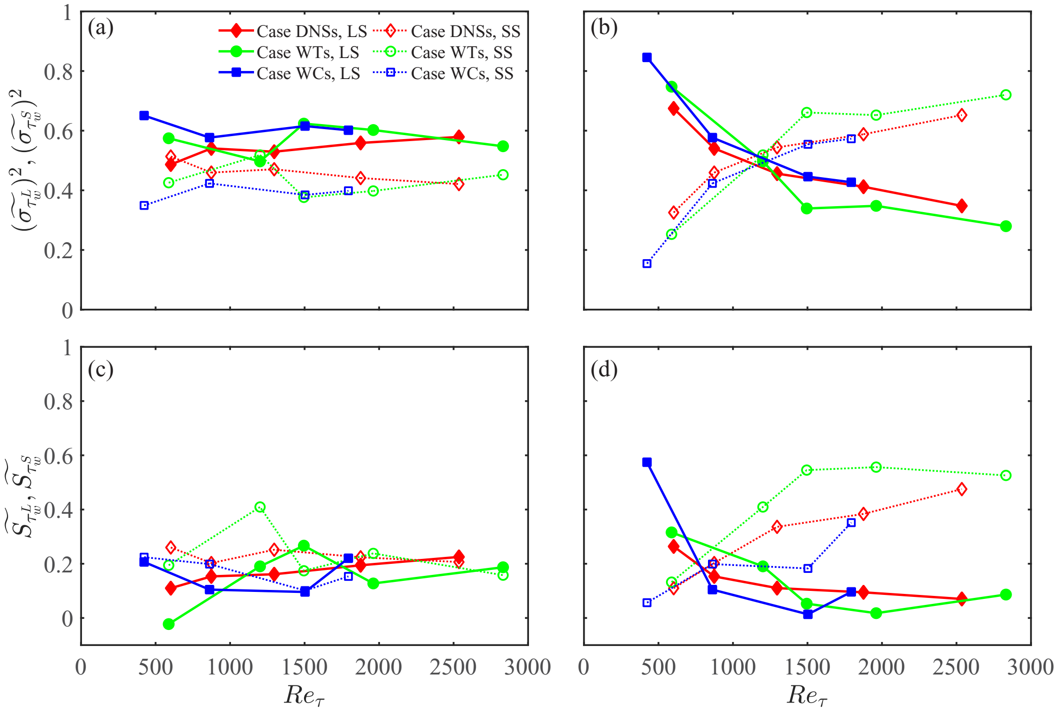

FIG. 16. The variance (a, b) and the skewness (c, d) of LS and SS as a function of Re_τ. (a, c) $\lambda_{xc}^+ = 1000$; (b, d) $\lambda_{xc} = \delta$.

fluctuation, which is directly related with WSS at the wall, can be formulated as a linear combination of the footprint of large-scale motions in the outer region and the amplitude-modulated 'universal' small-scale signal. Based on both this formulation and the conjecture that X_{II} is insensitive to Re, the weak Re-dependency of the PDF and the spectrum of WSS leads to a conjecture that outer-layer large-scale motions only apply rather weak footprint effect on WSS at the wall in the Re_τ range studied here. This might also provide a possible explanation for the log-law scaling of $\sigma_{\tau_w}^+ \sim \ln \mathrm{Re}_\tau$.

VI. CONCLUDING REMARKS

In summary, the present work investigates the statistics and multiscale characteristics of the streamwise component of WSS in a canonical TBL at low-to-moderate Re ($\mathrm{Re}_\tau = 400 \sim 2900$) obtained by both PIV and DNS. An algorithm of SRCC, together with an iterative fitting procedure to account for the unsteadiness of the viscous sublayer, is applied to get instantaneous WSS from time-resolved near-wall 2D PIV measurement. The precision of this method is empirically validated by a comparison of the statistics and spectral characteristics of the measured WSS to both the DNS dataset being analyzed here and those reported in the existing literatures.

The fluctuating intensity of WSS is found to be consistent with the empirical log-law correlation of $\sigma_{\tau_w}^+ \sim \ln \mathrm{Re}_\tau$, which reflects the inevitable influence of outer-layer LSMs/VSLMs on the wall. Spectral analysis shows that the relative energy contents of the LS components fail to present a distinct Re-dependency. This infers that LSMs/VSLMs might only leave weak footprint on the wall in the present studied Re_τ range. Instead, it is near-wall low-speed streaks that dominate the energetic length scales of WSS. Such a mild footprint effect is further supported by the Re-independency of the skewness ($S_{\tau_w} \approx 1$), the PDF of τ_w'/σ_{τ_w} and the inner-scaled convection speed of WSS ($\overline{u_c}^+ \approx 12$).

Scale decomposition analysis infers the existence of an "optimal" scale filter to separate the LS and the SS components of the fluctuating WSS. The cutting-off wavelength of this filter is about $\lambda_{xc}^{+} = 1000$, equivalent to the peak wavelength of the premultiplied streamwise spectrum. Using this filter, a weak Re-dependency of the second- and third-order moments of LS and SS is evident. This again implies the mild footprint effect of LSMs/VLSMs on WSS in the present limited Re range. On considering the constant-ratio contribution of LS and SS to the overall fluctuating energy of WSS, as well as the weak Re-dependency of the LS-to-SS amplitude modulation that can be inferred from the scale decomposition form of the skewness of WSS, the log-law scaling of $\sigma_{\tau_w}^{+} \sim \ln \mathrm{Re}_\tau$ might be mainly attributed to the amplitude modulation effect of LSMs/VLSMs, instead of their footprint effect. However, it is intriguing to see that the "optimal" scale-separation length scale for WSS does not follow an outer-scaling, as is commonly seen in the velocity fluctuations above the wall. It is possible that the strong shear within the viscous sublayer provides a shelter from outer-layer structures. In this sense, the kinematics and unsteady dynamics inside the viscous sublayer deserves a detailed study in the future.

Finally, it is stressed that although being supported by various aspects of the characteristics of WSS, the present inference, i.e., the outer-layer large-scale motions mainly apply amplitude modulation effect, instead of footprint effect, on WSS, is based on results in a rather limited Re range ($\mathrm{Re}_\tau < 3000$). To our knowledge, the physical explanation can be attributed to the near-wall viscous effect that shelters inviscid outer-layer motions from the viscous sublayer. However, on considering the increasing weight of the inner-outer layer interaction with the increase of Re_τ, further studies in high Re regime is needed to give a thorough evaluation for this inference.

ACKNOWLEDGMENTS

This work was supported by both the National Natural Science Foundation of China (Grants No. 11490552, No. 91852206, and No. 11721202).

[1] B. Dean and B. Bhushan, Shark-skin surfaces for fluid-drag reduction in turbulent flow: A review, Philos. Trans. A: Math. Phys. Eng. Sci. **368**, 4775 (2010).

[2] J. Jiménez, Coherent structures in wall-bounded turbulence, J. Fluid Mech. **842**, P1 (2018).

[3] I. Marusic, J. P. Monty, M. Hultmark, and A. J. Smits, On the logarithmic region in wall turbulence, J. Fluid Mech. **716**, R3 (2013).

[4] J. Jiménez, Turbulent flows over rough walls, Annu. Rev. Fluid Mech. **36**, 173 (2004).

[5] X. Wu, M. Cruickshank, and S. Ghaemi, Negative skin friction during transition in a zero-pressure-gradient flat-plate boundary layer and in pipe flows with slip and no-slip boundary conditions, J. Fluid Mech. **887**, A26 (2020).

[6] H. M. Nagib, K. A. Chauhan, and P. A. Monkewitz, Approach to an asymptotic state for zero pressure gradient turbulent boundary layers, Philos. Trans. R. Soc. A **365**, 755 (2007).

[7] M. de Giovanetti, Y. Hwang, and H. Choi, Skin-friction generation by attached eddies in turbulent channel flow, J. Fluid Mech. **808**, 511 (2016).

[8] W. Li, Y. Fan, D. Modesti, and C. Cheng, Decomposition of the mean skin-friction drag in compressible turbulent channel flows, J. Fluid Mech. **875**, 101 (2019).

[9] G. I. Park and P. Moin, Space-time characteristics of wall-pressure and wall-shear-stress fluctuations in wall-modeled large eddy simulation, Phys. Rev. Fluids **1**, 024404 (2016).

[10] X. I. A. Yang, G. I. Park, and P. Moin, Log-layer mismatch and modeling of the fluctuating wall stress in wall-modeled large-eddy simulations, Phys. Rev. Fluids **2**, 104601 (2017).

[11] M. Abbassi, W. Baars, N. Hutchins, and I. Marusic, Skin-friction drag reduction in a high-Reynolds-number turbulent boundary layer via real-time control of large-scale structures, Int. J. Heat Fluid Flow **67**, 30 (2017).

[12] P. H. Alfredsson, A. V. Johansson, J. H. Haritonidis, and H. Eckelmann, The fluctuating wall-shear stress and the velocity field in the viscous sublayer, Phys. Fluids **31**, 1026 (1988).

[13] B. Khoo, Y. Chew, and C. Teo, Near-wall hot-wire measurements Part II: Turbulence time scale, convective velocity and spectra in the viscous sublayer, Exp. Fluids **5**, 494 (2001).

[14] G. Kunkel and I. Marusic, An approximate amplitude attenuation correction for hot-film shear stress sensors, Exp. Fluids **34**, 285 (2003).

[15] J. Sheng, E. Malkiel, and J. Katz, Using digital holographic microscopy for simultaneous measurements of 3D near wall velocity and wall-shear stress in a turbulent boundary layer, Exp. Fluids **45**, 1023 (2008).

[16] S. Große and W. Schröder, High Reynolds number turbulent wind tunnel boundary layer wall-shear stress sensor, J. Turbul. **10**, N14 (2009).

[17] S. Obi, K. Inoue, T. Furukawa, and S. Masuda, Experimental study on the statistics of wall-shear stress in turbulent channel flows, Int. J. Heat Fluid Flow **17**, 187 (1996).

[18] N. Miyagi, M. Kimura, H. Shoji, A. Saima, C.-M. Ho, S. Tung, and Y.-C. Tai, Statistical analysis on wall-shear stress of turbulent boundary layer in a channel flow using micro-shear stress imager, Int. J. Heat Fluid Flow **21**, 576 (2000).

[19] L. Keirsbulck, L. Labraga, and M. Gad-el Hak, Statistical properties of wall-shear stress fluctuations in turbulent channel flows, Int. J. Heat Fluid Flow **37**, 1 (2012).

[20] P.-A. Gubian, J. Stoker, J. Medvescek, L. Mydlarski, and B. R. Baliga, Evolution of wall-shear stress with Reynolds number in fully developed turbulent channel flow experiments, Phys. Rev. Fluids **4**, 074606 (2019).

[21] Y. Liu, M. Klaas, and W. Schröder, Measurements of the wall-shear stress distribution in turbulent channel flow using the micropillar shear stress sensor mps3, Exp. Therm. Fluid Sci. **106**, 171 (2019).

[22] P. Schlatter and R. Örlü, Assessment of direct numerical simulation data of turbulent boundary layers, J. Fluid Mech. **659**, 116 (2010).

[23] H. Abe, H. Kawamura, and H. Choi, Very large-scale structures and their effects on the wall-shear-stress fluctuations in a turbulent channel flow up to $Re_\tau = 640$, J. Fluids Eng. **126**, 835 (2004).

[24] Z. Hu, C. L. Morfey, and N. D. Sandham, Wall pressure and shear stress spectra from direct simulations of channel flow, AIAA J. **44**, 1541 (2006).

[25] M. Lee and R. D. Moser, Direct numerical simulation of turbulent channel flow up to $Re_\tau \approx 5200$, J. Fluid Mech. **774**, 395 (2015).

[26] C. Diaz-Daniel, S. Laizet, and J. C. Vassilicos, Wall-shear stress fluctuations: Mixed scaling and their effects on velocity fluctuations in a turbulent boundary layer, Phys. Fluids **29**, 055102 (2017).

[27] N. Hutchins, J. P. Monty, B. Ganapathisubramani, H. C.-H. Ng, and I. Marusic, Three-dimensional conditional structure of a high-Reynolds-number turbulent boundary layer, J. Fluid Mech. **673**, 255 (2011).

[28] R. Örlü and P. Schlatter, On the fluctuating wall-shear stress in zero pressure-gradient turbulent boundary layer flows, Phys. Fluids **23**, 021704 (2011).

[29] R. Mathis, I. Marusic, S. I. Chernyshenko, and N. Hutchins, Estimating wall-shear-stress fluctuations given an outer region input, J. Fluid Mech. **715**, 163 (2013).

[30] J. M. Österlund, *Experimental Studies of Zero Pressure-gradient Turbulent Boundary Layer Flow*, Ph.d. thesis, Mekanik (1999).

[31] C. E. Willert, High-speed particle image velocimetry for the efficient measurement of turbulence statistics, Exp. Fluids **56**, 17 (2015).

[32] W. Li, D. Roggenkamp, W. Jessen, M. Klaas, and W. Schröder, Reynolds number effects on the fluctuating velocity distribution in wall-bounded shear layers, Meas. Sci. Technol. **28**, 015302 (2016).

[33] M., Aguiar, Ferreira, E., Rodriguez-Lopez, B., and Ganapathisubramani, An alternative floating element design for skin-friction measurement of turbulent wall flows, Exp. Fluids **59**, 155 (2018).

[34] D. A. Mills, C. Barnard, and M. Sheplak, Characterization of a hydraulically smooth wall-shear stress sensor for low-speed wind tunnel applications, in *Proceedings of the 55th AIAA Aerospace Sciences Meeting, AIAA SciTech Forum* (2017).

[35] R. Savelsberg, M. Schiffer, E. Obermeier, and I. P. Castro, Calibration and use of a MEMS surface fence for wall-shear stress measurements in turbulent flows, Exp. Fluids **53**, 489 (2012).

[36] J. W. Naughton and M. Sheplak, Modern developments in shear-stress measurement, Prog. Aerospace Sci. **38**, 515 (2002).

[37] T. J. Hanratty and J. A. Campbell, Measurement of wall-shear stress, in *Fluid Mechanics Measurements* (Routledge, London, 2017), pp. 575–648.

[38] X. Liu, Z. Li, C. Wu, and N. Gao, Toward calibration-free wall-shear stress measurement using a dual hot-film sensor and Kelvin bridges, Meas. Sci. Technol. **29**, 105303 (2018).

[39] N. Hutchins and K.-S. Choi, Accurate measurements of local skin friction coefficient using hot-wire anemometry, Prog. Aerospace Sci. **38**, 421 (2002).

[40] R. Örlü, J. H. Fransson, and P. H. Alfredsson, On near wall measurements of wall bounded flows-the necessity of an accurate determination of the wall position, Prog. Aerospace Sci. **46**, 353 (2010).

[41] C. J. Kähler, U. Scholz, and J. Ortmanns, Wall-shear-stress and near-wall turbulence measurements up to single pixel resolution by means of long-distance micro-PIV, Exp. Fluids **41**, 327 (2006).

[42] T. D. Nguyen, J. C. Wells, and C. V. Nguyen, Wall-shear stress measurement of near-wall flow over inclined and curved boundaries by stereo interfacial particle image velocimetry, Int. J. Heat Fluid Flow **31**, 442 (2010).

[43] J. Shen, C. Pan, and J. Wang, Accurate measurement of wall skin friction by single-pixel ensemble correlation, Sci. China: Phys., Mech. Astron. **57**, 1352 (2014).

[44] Y. Zhu, X. Jiang, Y. Zhang, and C. Lee, Iterative PIV interrogation for complex wall-bounded flows, Meas. Sci. Technol. **30**, 095302 (2019).

[45] W. A. Rowin and S. Ghaemi, Streamwise and spanwise slip over a superhydrophobic surface, J. Fluid Mech. **870**, 1127 (2019).

[46] M. Novara, D. Schanz, N. Reuther, C. J. Kähler, and A. Schröder, Lagrangian 3D particle tracking in high-speed flows: Shake-the-box for multi-pulse systems, Exp. Fluids **57**, 128 (2016).

[47] C. V. Nguyen and J. C. Wells, Direct measurement of fluid velocity gradients at a wall by PIV image processing with stereo reconstruction, J. Visualization **9**, 199 (2006).

[48] C. V. Nguyen, T. D. Nguyen, J. C. Wells, and A. Nakayama, Interfacial PIV to resolve flows in the vicinity of curved surfaces, Exp. Fluids **48**, 577 (2010).

[49] M. P. Simens, J. Jiménez, S. Hoyas, and Y. Mizuno, A high-resolution code for turbulent boundary layers, J. Comput. Phys. **228**, 4218 (2009).

[50] J. A. Sillero, J. Jiménez, and R. D. Moser, One-point statistics for turbulent wall-bounded flows at Reynolds numbers up to $\delta^+ \approx 2000$, Phys. Fluids **25**, 105102 (2013).

[51] J. A. Sillero, J. Jiménez, and R. D. Moser, Two-point statistics for turbulent boundary layers and channels at Reynolds numbers up to $\delta^+ \approx 2000$, Phys. Fluids **26**, 105109 (2014).

[52] W. Wang, C. Pan, and J. Wang, Quasibivariate variational mode decomposition as a tool of scale analysis in wall-bounded turbulence, Exp. Fluids **59**, 1 (2018).

[53] W. Wang, C. Pan, and J. Wang, Multi-component variational mode decomposition and its application on wall-bounded turbulence, Exp. Fluids **60**, 95 (2019).

[54] W. Wang, C. Pan, and J. Wang, Wall-normal variation of spanwise streak spacing in turbulent boundary layer with low-to-moderate Reynolds number, Entropy **21**, 24 (2019).

[55] S. Grosse and W. Schröder, Wall-shear stress patterns of coherent structures in turbulent duct flow, J. Fluid Mech. **633**, 147 (2009).

[56] S. Deng, C. Pan, J. Wang, and G. He, On the spatial organization of hairpin packets in a turbulent boundary layer at low-to-moderate Reynolds number, J. Fluid Mech. **844**, 635 (2018).

[57] K. A. Chauhan, P. A. Monkewitz, and H. M. Nagib, Criteria for assessing experiments in zero pressure gradient boundary layers, Fluid Dynam. Res. **41**, 021404 (2009).

[58] R. Baidya, J. Philip, N. Hutchins, J. Monty, and I. Marusic, Distance-from-the-wall scaling of turbulent motions in wall-bounded flows, Phys. Fluids **29**, 020712 (2017).

[59] P. A. Monkewitz, K. A. Chauhan, and H. M. Nagib, Self-consistent high-Reynolds-number asymptotics for zero-pressure-gradient turbulent boundary layers, Phys. Fluids **19**, 115101 (2007).

[60] K. Okamoto, S. Nishio, T. Saga, and T. Kobayashi, Standard images for particle-image velocimetry, Meas. Sci. Technol. **11**, 685 (2000).

[61] J. Westerweel, P. Geelhoed, and R. Lindken, Single-pixel resolution ensemble correlation for micro-PIV applications, Exp. Fluids **37**, 375 (2004).

[62] C. J. Kähler, S. Scharnowski, and C. Cierpka, On the resolution limit of digital particle image velocimetry, Exp. Fluids **52**, 1629 (2012).

[63] Q. Zhou and K.-Q. Xia, Measured Instantaneous Viscous Boundary Layer in Turbulent Rayleigh-Bénard Convection, Phys. Rev. Lett. **104**, 104301 (2010).

[64] C. Pan and Y. Kwon, Extremely high wall-shear stress events in a turbulent boundary layer, in *Journal of Physics: Conference Series*, Vol. 1001 (IOP Publishing, Bristol, UK, 2018), p. 012004.

[65] P. Lenaers, Q. Li, G. Brethouwer, P. Schlatter, and R. ÖRlü, Rare backflow and extreme wall-normal velocity fluctuations in near-wall turbulence, Phys. Fluids **24**, 035110 (2012).

[66] C. E. Willert, C. Cuvier, J. M. Foucaut, J. Klinner, M. Stanislas, J. P. Laval, S. Srinath, J. Soria, O. Amili, C. Atkinson, C. J. Kähler, S. Scharnowski, R. Hain, A. Schröder, R. Geisler, J. Agocs, and A. Röse, Experimental evidence of near-wall reverse flow events in a zero pressure gradient turbulent boundary layer, Exp. Therm. Fluid Sci. **91**, 320 (2018).

[67] S. Herpin, M. Stanislas, J. M. Foucaut, and S. Coudert, Influence of the Reynolds number on the vortical structures in the logarithmic region of turbulent boundary layers, J. Fluid Mech. **716**, 5 (2013).

[68] X. Yang and M. Howland, Implication of Taylor's hypothesis on measuring flow modulation, J. Fluid Mech. **836**, 222 (2018).

[69] J. C. Del Álamo and J. Jiménez, Estimation of turbulent convection velocities and corrections to Taylor's approximation, J. Fluid Mech. **640**, 5 (2009).

[70] J. Monty and M. Chong, Turbulent channel flow: Comparison of streamwise velocity data from experiments and direct numerical simulation, J. Fluid Mech. **633**, 461 (2009).

[71] S. Jeon, H. Choi, J. Y. Yoo, and P. Moin, Space–time characteristics of the wall-shear-stress fluctuations in a low-Reynolds-number channel flow, Phys. Fluids **11**, 3084 (1999).

[72] R. Mathis, N. Hutchins, and I. Marusic, Large-scale amplitude modulation of the small-scale structures in turbulent boundary layers, J. Fluid Mech. **628**, 311 (2009).

[73] P. Schlatter and R. Örlü, Quantifying the interaction between large and small scales in wall-bounded turbulent flows: A note of caution, Phys. Fluids **22**, 051704 (2010).

[74] K. Talluru, R. Baidya, N. Hutchins, and I. Marusic, Amplitude modulation of all three velocity components in turbulent boundary layers, J. Fluid Mech. **746**, R1 (2014).

[75] H. Liu, G. Wang, and X. Zheng, Amplitude modulation between multiscale turbulent motions in high-Reynolds-number atmospheric surface layers, J. Fluid Mech. **861**, 585 (2019).

[76] R. Mathis, I. Marusic, N. Hutchins, and K. Sreenivasan, The relationship between the velocity skewness and the amplitude modulation of the small scale by the large scale in turbulent boundary layers, Phys. Fluids **23**, 121702 (2011).

[77] S. Duvvuri and B. J. McKeon, Triadic scale interactions in a turbulent boundary layer, J. Fluid Mech. **767**, R4 (2015).

[78] I. Marusic, R. Mathis, and N. Hutchins, Predictive model for wall-bounded turbulent flow, Science **329**, 193 (2010).